J Dominski et al.

An arbitrary wavelength solver for global gyrokinetic simulations. Application to the study of fine radial structures on microturbulence due to non-adiabatic passing electron dynamics

An arbitrary wavelength solver for global gyrokinetic simulations. Application to the study of fine radial structures on microturbulence due to nonadiabatic passing electron dynamics

J Dominski,[1, a)] B.F. McMillan,[2] S. Brunner,[1] G. Merlo,[1] T.-M. Tran,[1] and L. Villard[1]

[1)] *École Polytechnique Fédérale de Lausanne, Swiss Plasma Center,*
CH-1015 Lausanne, Switzerland.

[2)] *Warwick university.*

(Dated: 1 June 2016)

A new arbitrary wavelength solver to the gyrokinetic quasi-neutrality equation is implemented in the gyrokinetic code ORB5. This new solver accounts for the polarization drift term contribution to the quasi-neutrality equation in its integral form, and is thus valid for arbitrary wavelength compared to the ion thermal Larmor radius. This new feature of the ORB5 code overcomes the former long-wavelength approximation made in the original version of the code. This effort is made to pursue the study of the influence of the nonadiabatic passing electron response near mode rational surfaces in global geometry. A Padé approximation version has also been implemented and is systematically compared to the results obtained with the arbitrary wavelength version of the solver. A benchmark is conducted against the global version of the gyrokinetic code GENE, showing very good agreement. First nonlinear simulations are carried out in condition relevant for the TCV tokamak, shot #45353, with the physical Deuterium to electron mass ratio ($m_i/m_e = 3672$) and are compared to simulations carried out with heavy electrons ($m_i/m_e = 400$). The particular spectral organization of the passing electron turbulent flux is revealed, showing strong ties with the radial profile of safety factor. In particular, the formation of transport barriers is studied near low order mode rational. These nonlinear simulations show that realistic nonlinear fully-kinetic simulations of tokamak transport must be carried out in a full torus and with the real mass ratio.

[a)]julien.dominski@epfl.ch

I.   INTRODUCTION

The micro-turbulence occurring in the core of tokamak magnetic confinement experiments is known to be responsible for important losses of heat and particles. These losses are essentially due to the turbulent transport caused by instabilities of various types, as for example the ion temperature gradient (ITG) modes, the trapped electron modes (TEM), or the electron temperature gradient (ETG) modes. The dynamics of these regimes have different characteristic length and time scales and because these modes coexist in a fusion plasma, plasma turbulence is a multi-scale problem[1–4]. The multi-scale nature of plasma dynamics can also be observed in purely electrostatic ITG or TEM regimes when resolving the kinetic passing electron dynamics at short scales[5], *i.e.* $\lesssim \rho_i$. In such case, illustrated in the present work, it appears that fine radial structures due to the nonadiabatic response of passing electrons are present near low-order mode rational surfaces over the electrostatic potential, the species density and temperatures. The presence of these fine structures alter the zonal flows and the level of turbulence transport. Multi-scales simulations are thus obviously required for accurate prediction of tokamak plasma confinement properties.

To enable carrying out such multi-scale simulations in global geometries with the gyrokinetic code ORB5, a new arbitrary-wavelength (compared to the ion Larmor radius) electrostatic-field solver has been implemented. This new feature of the ORB5 code overcomes the former long-wavelength approximation made in the original version of the code, see Refs. 6 and 7. The gyrokinetic code ORB5 is today a multi-scale, multispecies, collisional, electromagnetic, and global gyrokinetic PIC code, in which the statistical numerical noise is controlled using modified Krook operators or coarse graining procedures. The main steps which led to the current state of the code are: an electromagnetic version[8] sometimes referred to as NEMORB, the inclusion of new sources and noise control[9], a field-aligned Fourier solver[10], inter- and intra-species collisions[11], and the effect of strong flows[12].

We present in this paper first ORB5 results obtained with this new generalized field solver, based on the finite-element representation of the field[6,13]. In this solver, the linearized polarization drift contribution to the quasi-neutrality equation (QNE) is accounted for in its integral form by following a similar method to Ref. 14. The main differences are that the kernel of the integral solver is integrated making use of an Eulerian grid instead of a Monte-Carlo-type integration, and that the field is solved for the discrete Fourier representation

of its finite-element coefficients. This discrete Fourier representation significantly reduces the size of the corresponding matrix system[10]. A Padé version of the solver has also been implemented and is compared to the integral solver. Initial comparison of such a Padé approximation with a generalized solver was initially done in Ref. 15, where a generalized electrostatic field solver was also presented. The main difference of the here presented arbitrary wavelength solver with the one in Ref. 15, as already pointed in Ref. 14, is that the temperature and density are not assumed constant when doing the gyroaveraging operation for assembling the ion polarization drift contribution to the QNE.

The remainder of this paper is organized as follows. In section II, the new field solver valid for arbitrary wavelength is introduced. In section III, a linear benchmark is carried out with ORB5 against the global version of the gyrokinetic code GENE[16,17] in global realistic MHD geometry considering the three electron models[5]: adiabatic, hybrid, and kinetic. In section IV, nonlinear simulations for conditions relevant to TCV[18] are performed with fully-kinetic electrons and the arbitrary wavelength solver. Results obtained with the integral solver are compared to the Padé approximation version. The different contributions of sub- and suprathermal particle species to the fluxes and their radial organization, involving in particular zonal flows structures in the vicinity of MRSs are studied in detail.

II. THE ARBITRARY WAVELENGTH SOLVER

A. Quasi-neutrality equation

The quasi-neutrality equation reads $\sum_\sigma q_\sigma N_\sigma = 0$ with q_σ the electric charge and N_σ the density of the different species, σ, composing the plasma. In the frame of a gyrokinetic description[19], each species density is computed from equation

$$N_\sigma(\mathbf{x}; t) = \int d\mathbf{Z}\, \delta(\mathbf{X} + \boldsymbol{\rho} - \mathbf{x}) \left(f_\sigma + \frac{q_\sigma}{B_0}\tilde{\phi}\frac{\partial f_\sigma}{\partial \mu} \right), \tag{1}$$

where the electrostatic potential $\phi = \delta\phi$ is a pure perturbation, $\mathbf{x}$ a position in configuration space, $f_\sigma(\mathbf{X}, v_\perp, \mu; t)$ the particle distribution function in gyrocenter variables which is evolved according to the gyrokinetic equation[20], $\mathbf{X}$ the guiding center, $\boldsymbol{\rho} = \boldsymbol{\rho}(\mathbf{X}, \mu, \alpha)$ the Larmor vector, α the gyro-angle, $\mu = m_\sigma v_\perp^2/2B_0$ the magnetic moment, $v_\perp$ the particle velocity component perpendicular to the magnetic field, $v_\parallel$ the velocity component parallel to the magnetic field, $d\mathbf{Z} = d\mathbf{X}dv_\parallel d\mu d\alpha(B_{0\parallel}^\star/m_\sigma)$ the infinitesimal phase-space volume in

guiding-center coordinates $(\mathbf{X}, v_\parallel, \mu, \alpha)$, $B^\star_{0\parallel} = B_0 + (m_\sigma/q_\sigma)v_\parallel \mathbf{b} \cdot \nabla \times \mathbf{b}$, B_0 the equilibrium magnetic field amplitude, $\mathbf{b} = \mathbf{B}_0/B_0$, and $\delta(\mathbf{X} + \boldsymbol{\rho} - \mathbf{x})$ the Dirac delta function. The polarization term is explicitly function of the electrostatic field ϕ through the term $\tilde{\phi}(\mathbf{X}, \mu, \alpha) = \delta\phi(\mathbf{X} + \boldsymbol{\rho}) - \langle\delta\phi\rangle_\alpha(\mathbf{X}, \mu)$ with

$$\langle\delta\phi\rangle_\alpha(\mathbf{X}, \mu) = \oint \frac{d\alpha}{2\pi}\delta\phi(\mathbf{X} + \boldsymbol{\rho}), \tag{2}$$

standing for the gyro-averaged field. Note that the norm of the Larmor vector is $\rho_\sigma(\mathbf{X}, \mu) = v_\perp/\Omega_{\sigma0}(\mathbf{X})$ with $\Omega_{\sigma0}(\mathbf{X}) = q_\sigma B_0(\mathbf{X})/m_\sigma$ the cyclotron frequency and m_σ the species mass. Moreover, the species thermal Larmor radius is defined by $\rho_{\mathrm{th,j}}(\mathbf{x}) = v_{\mathrm{th,j}}(\mathbf{x})/\Omega_{\sigma0}(\mathbf{x})$ with $v_{\mathrm{th,j}}(\mathbf{x}) = \sqrt{T_{\sigma0}(\mathbf{x})/m_\sigma}$ the thermal velocity, and $T_{\sigma0}(\mathbf{x})$ the species background temperature. The ion sound Larmor radius is $\rho_s(\mathbf{x}) = c_s(\mathbf{x})/\Omega_{i0}(\mathbf{x})$ with $c_\mathrm{s}(\mathbf{x}) = \sqrt{Z_i T_{e0}(\mathbf{x})/m_i}$ the ion sound speed of the ion species i with ionization degree Z_i.

As the background plasma is assumed neutral, $\sum_\sigma q_\sigma N_{\sigma0}(\mathbf{x}) = 0$, the quasi-neutrality equation can then be rewritten by keeping only the perturbation terms $\sum_\sigma q_\sigma \delta N_\sigma(\mathbf{x}; t) = 0$, where the particle distribution function f_σ is split in a time-independent background, $f_{\sigma0}$, and a time-dependent perturbation, δf_σ, such that $f_\sigma(\mathbf{X}, v_\parallel, \mu; t) = f_{\sigma0}(\mathbf{X}, v_\parallel, \mu) + \delta f_\sigma(\mathbf{X}, v_\parallel, \mu; t)$. From Eq. (1), the background density is

$$N_{\sigma0}(\mathbf{x}) = \int d\mathbf{Z}\, \delta(\mathbf{X} + \boldsymbol{\rho} - \mathbf{x})f_{\sigma0}(\mathbf{X}, v_\parallel, \mu), \tag{3}$$

and the perturbation density is composed of two terms: the gyro-density contribution

$$\delta N_\sigma^{\mathrm{gy}}(\mathbf{x}; t) = \int d\mathbf{Z}\, \delta(\mathbf{X} + \boldsymbol{\rho} - \mathbf{x})\delta f_\sigma(\mathbf{X}, v_\parallel, \mu; t), \tag{4}$$

and the linearized polarization-drift contribution

$$\delta N_\sigma^{\mathrm{pol}}(\mathbf{x}; t) = \int d\mathbf{Z}\, \delta(\mathbf{X} + \boldsymbol{\rho} - \mathbf{x})\frac{q_\sigma}{B_0(\mathbf{X})}\delta\tilde{\phi}(\mathbf{X}, \mu; t)\frac{\partial f_{\sigma0}(\mathbf{X}, v_\parallel, \mu)}{\partial\mu}, \tag{5}$$

such that $\delta N_\sigma = \delta N_\sigma^{gy} + \delta N_\sigma^{pol}$ and having neglected the nonlinear contribution to the polarization density.

In the present work, different approximations and models are considered for the perturbation density, which we will briefly list here. For *ion species* and for sufficiently long wavelengths with respect to the ion Larmor radius, $k_\perp \rho_i \ll 1$, with $k_\perp$ the perturbation wavenumber in the direction perpendicular to the magnetic field, the so-called long-wavelength approximation may be considered for estimating

$$\delta N_i^{\mathrm{pol}}(\mathbf{x}; t) \simeq \frac{q_i}{m_i}\nabla_\perp \cdot \frac{N_{i0}(\mathbf{x})}{\Omega_{i0}^2(\mathbf{x})}\nabla_\perp\delta\phi(\mathbf{x}; t), \tag{6}$$

4

with $q_i = eZ_i$ the ion charge and e the elementary electric charge. This approximation was made in the previous versions of the gyrokinetic code ORB5[6–8]. For the present work, a new field solver is implemented in the ORB5 code, for which the linear polarization contribution to the perturbed density is computed from the integral form as described in Eq. (5). Note that, as an improvement over the long-wavelength approximation Eq. (6), a Padé approximation version of this integral solver has been implemented as well, for which the ion polarization drift term is estimated using the relation

$$\delta N_i^{\text{pol}}(\mathbf{x}; t) \simeq \left[1 - \nabla_\perp \cdot \rho_i^2(\mathbf{x}) \nabla_\perp \right]^{-1} \left[\frac{eZ_i}{m_i} \nabla_\perp \cdot \frac{N_{i0}(\mathbf{x})}{\Omega_{i0}^2(\mathbf{x})} \nabla_\perp \delta\phi(\mathbf{x}; t) \right]. \tag{7}$$

This approximation is based on the expression of the polarization drift term in Fourier space for a homogeneous plasma[15,21] $\delta\hat{N}_i^{\text{pol}}(\mathbf{k}) = (qN_{i0}/T_{i0}) \left[1 - \Lambda_0(k_\perp^2 \rho_{th,i}^2) \right] \delta\hat{\phi}(\mathbf{k})$ and on the Padé approximation of the scaled modified Bessel function of order zero $\Lambda_0(\xi) = e^{-\xi} I_0(\xi) \simeq 1/(1 + \xi)$. In practice, the operator $[1 - \nabla_\perp \cdot \rho_i^2 \nabla_\perp]$ is applied to all terms of the QNE effectively canceling the operator $[1 - \nabla_\perp \cdot \rho_i^2 \nabla_\perp]^{-1}$ in Eq. (7). For *electrons* and for small wavelengths with respect to the ion Larmor radius, $k_\perp \rho_i \gtrsim 1$, but still sufficiently long with respect to the electron Larmor radius, $k_\perp \rho_e \ll 1$, the drift-kinetic approximation can be made. It consists in neglecting the electron polarization term, Eq. (5), reducing the electron perturbed density to its gyro-density in which the Larmor radius is taken to be zero

$$\delta N_e(\mathbf{x}; t) \simeq \delta N_e^{\text{gy}}(\mathbf{x}; t) \simeq \int d\mathbf{Z} \, \delta f_e(\mathbf{x}, \mu, v_\parallel; t). \tag{8}$$

For certain types of fluctuations the electron response can also be computed from the adiabatic (Boltzmann) approximation[22]

$$\delta N_e^{\text{ad}}(\mathbf{x}; t) = \frac{eN_{0e}}{T_{0e}} \left[\delta\phi(\mathbf{x}; t) - \langle \delta\phi \rangle_{FS}(s; t) \right], \tag{9}$$

where $\langle \delta\phi \rangle_{FS}(s) = \int d\varphi d\theta^\star \mathcal{J} \delta\phi / \int d\varphi d\theta^\star \mathcal{J}$ is the flux-surface average of the perturbed electrostatic potential expressed in magnetic coordinates $(s, \theta^\star, \varphi)$ with s the flux-surface label, $\theta^\star$ the straight field line poloidal angle, φ the periodic toroidal direction, and $\mathcal{J}$ the associated Jacobian. Finally, a hybrid model can also be considered, in which the trapped electrons are described kinetically and the passing electrons are described adiabatically $\delta N_e^{\text{hyb}}(\mathbf{x}) = \delta N_{e,\text{trp}}^{\text{kin}}(\mathbf{x}) + \delta N_{e,\text{pas}}^{\text{ad}}(\mathbf{x})$. More details concerning these electron models are given in Refs. 5 and 23.

Considering the different possible electron models and approximations, the most general form of the quasi-neutrality equation can be written

$$-\sum_{\sigma\in\{\text{kin}\}} q_\sigma \int d\mathbf{Z}\delta(\mathbf{X}+\boldsymbol{\rho}-\mathbf{x})\delta\tilde{\phi}\frac{q_\sigma}{B_0}\frac{\partial f_{\sigma 0}}{\partial\mu} + \sum_{\sigma\in\{\text{ad}\}} q_\sigma N_{\sigma 0}\frac{q_\sigma(\delta\phi-\langle\delta\phi\rangle_{FS})}{T_{\sigma 0}} = \sum_{\sigma\in\{\text{kin}|\text{dk}\}} q_\sigma\delta N_\sigma^{\text{gy}},$$

(10)

where one uses the sets {kin}, {ad}, and {kin|dk} to denote the (subgroup) species which are modeled kinetically, adiabatically, and either kinetically or drift-kinetically, respectively.

B. Discretized QNE

In this section, the Ritz-Galerkin method is used to project the quasi-neutrality equation (QNE) on a set of finite-elements $\{\Lambda_\nu(\mathbf{x})\}$, such that this integral equation is transformed into a system of linear equations[6,13]

$$\sum_{\nu'} L_{\nu\nu'}\delta\phi_{\nu'} = S_\nu,$$

(11)

where $L_{\nu\nu'}\delta\phi_{\nu'}$ and S_ν are, respectively, the Galerkin projections, $\int d\mathbf{x}\Lambda_\nu(\mathbf{x})...$, of the left and right hand sides of Eq. (10). The unknown terms $\delta\phi_{\nu'}$ in this system of linear equations are the coefficients of the finite-element representation of the electrostatic field

$$\delta\phi(\mathbf{x}) = \sum_{\nu'}\delta\phi_{\nu'}\Lambda_{\nu'}(\mathbf{x}).$$

(12)

The source term S_ν is the projection of the gyro-density

$$S_\nu = 2\pi\sum_{\sigma\in\{\text{kin}|\text{dk}\}} q_\sigma\int d\mathbf{X}dv_\parallel d\mu\frac{B_{0\parallel}^\star}{m_\sigma}\langle\Lambda_\nu\rangle_\alpha(\mathbf{X},\mu)\delta f_\sigma(\mathbf{X},\mu,v_\parallel),$$

(13)

where one performed the simplification $\int d\mathbf{x}\Lambda_\nu(\mathbf{x})\delta(\mathbf{X}+\boldsymbol{\rho}-\mathbf{x}) \equiv \Lambda_\nu(\mathbf{X}+\boldsymbol{\rho})$. In PIC representation, as considered in the ORB5 code[6], this source term is computed from the marker particles

$$S_\nu = \sum_p q_p w_p(t)\langle\Lambda_\nu\rangle_\alpha(\mathbf{X}_p,\mu_p),$$

(14)

with p the subscript labeling the particle quantities and w_p the particle weight. Finally, the matrix $L_{\nu\nu'}$ is composed of the linearized polarization-drift contribution(s), $L_{\nu\nu'}^{\text{pol}}$, as well as of the possibly adiabatic electron response, $L_{\nu\nu'}^{\text{ad}}$, with $L_{\nu\nu'} = L_{\nu\nu'}^{\text{pol}} + L_{\nu\nu'}^{\text{ad}}$.

The *adiabatic response* matrix reads

$$L_{\nu\nu'}^{\mathrm{ad}} = - \sum_{\sigma\in\{\mathrm{ad}\}} q_\sigma^2 \int d\mathbf{x} \frac{N_{\sigma 0}(\mathbf{x})}{T_{\sigma 0}(\mathbf{x})} \Lambda_\nu(\mathbf{x}) \left[\Lambda_{\nu'}(\mathbf{x}) - \langle\Lambda_{\nu'}\rangle_{FS}(s)\right], \tag{15}$$

with $\{\mathrm{ad}\}$ the set of species sub-groups which are modeled adiabatically, see Eq. (10).

The *arbitrary-wavelength* polarization matrix, related to the term defined in Eq. (5), reads

$$L_{\nu\nu'}^{\mathrm{pol}} = 2\pi \sum_{\sigma\in\{\mathrm{kin}\}} q_\sigma \int d\mathbf{X} dv_\parallel d\mu \frac{B_{0\parallel}^\star}{m_\sigma} \frac{q_\sigma}{B_0} \left(-\frac{\partial f_{\sigma 0}}{\partial \mu}\right) \left[\langle\Lambda_\nu\Lambda_{\nu'}\rangle_\alpha - \langle\Lambda_\nu\rangle_\alpha\langle\Lambda_{\nu'}\rangle_\alpha\right], \tag{16}$$

where $\langle\Lambda_\nu\rangle_\alpha = \langle\Lambda_\nu\rangle_\alpha(\mathbf{X},\mu)$. This latter matrix is symmetric and positive definite because it is the positively weighted $(-\partial f_{\sigma 0}/\partial\mu > 0)$ sum of the symmetric and positive definite sub-matrices $P_{\nu\nu'} = \langle\Lambda_\nu\Lambda_{\nu'}\rangle_\alpha - \langle\Lambda_\nu\rangle_\alpha\langle\Lambda_{\nu'}\rangle_\alpha$ ($P = P^t$ and $\langle\phi^2\rangle_\alpha \geq \langle\phi\rangle_\alpha^2$ for all ϕ).

The *long-wavelength* polarization matrix, defined by Eq. (6), reads

$$L_{\nu\nu'}^{\mathrm{pol}} = \sum_{\sigma\in\{\mathrm{kin}\}} \frac{q_\sigma^2}{m_\sigma} \int d\mathbf{x} \frac{N_{\sigma 0}(\mathbf{x})}{\Omega_{\sigma 0}^2(\mathbf{x})} \nabla_\perp\Lambda_\nu(\mathbf{x})\nabla_\perp\Lambda_{\nu'}(\mathbf{x}), \tag{17}$$

where one has performed an integration by parts of the form

$$\int d\mathbf{x}\Lambda_\nu(\nabla_\perp F\nabla_\perp\Lambda_{\nu'}) = [\Lambda_\nu F\nabla_\perp\Lambda_{\nu'}]_{\partial\Omega} - \int d\mathbf{x}\nabla_\perp\Lambda_\nu\ F\nabla_\perp\Lambda_{\nu'},$$

and the term $[\Lambda_\nu F\nabla_\perp\Lambda_{\nu'}]_{\partial\Omega} = 0$ as a result of imposed Dirichlet boundary conditions. Note that no boundary conditions need to be imposed for deriving the matrix in the finite element representation of the integral operator, Eq. (16). The behavior of the solutions to the QNE at the boundary will be discussed in more details in Sec. II F.

C. Discretized QNE in the particular case of the Padé approximation

The Padé approximation version of the QNE of a two species plasma with drift-kinetic electrons, reads

$$-\frac{q_i^2}{m_i}\nabla_\perp \cdot \frac{N_{i0}}{\Omega_{i0}^2}\nabla_\perp\phi = (1 - \nabla_\perp \cdot \rho_i^2\nabla_\perp) \sum_{\sigma=\{i,e\}} q_\sigma \int d\mathbf{Z}\delta(\mathbf{X}+\boldsymbol{\rho}_\sigma-\mathbf{x})\delta f_\sigma, \tag{18}$$

where $|\boldsymbol{\rho}_e| = 0$ and $q_e = -e$. Compared to the long wavelength version of the solver, the difference is the presence of the operator $(1 - \nabla_\perp \cdot \rho_i^2\nabla_\perp)$ on the RHS of Eq. (18). This

operator effectively necessitates the computation of an additional source term on the RHS of Eq. (11), which now reads $\sum_{\nu'} L^{\text{pol}}_{\nu\nu'}\delta\phi_{\nu'} = S_\nu + S^{\text{corr}}_\nu$ with $S^{\text{corr}}_\nu = L^{\text{corr}}_{\nu\nu'}s_{\nu'}$ and

$$L^{\text{corr}}_{\nu\nu'} = -\sum_{\nu'} \int d\mathbf{x}\, \rho^2_{\text{th,i}}(\mathbf{x})\nabla_\perp\Lambda_\nu(\mathbf{x})\nabla_\perp\Lambda_{\nu'}(\mathbf{x}) \tag{19}$$

where an integration by parts and Dirichlet boundary conditions have been used, and the s_ν stand for the coefficients of the decomposition into finite elements of the total gyro-density: $\sum_{\nu'} s_{\nu'}\Lambda_{\nu'}(\mathbf{x}) = \sum_s q_s \int d\mathbf{Z}\delta(\mathbf{X} + \boldsymbol{\rho}_s - \mathbf{x})\delta f_s$. The above relation can be inverted for s_ν by projection onto the basis elements $\Lambda_\nu(\mathbf{x})$ and making use of the definition (13) of S_ν, leading to

$$s_{\nu'} = M^{-1}_{\nu\nu'}S_\nu, \tag{20}$$

where $M_{\nu\nu'} = \int d\mathbf{x}\Lambda_\nu(\mathbf{x})\Lambda_{\nu'}(\mathbf{x})$ is the mass matrix. In this Padé version of the solver, the RHS of the QNE is $S^{\text{Pade}}_\nu = S_\nu + S^{\text{corr}}_\nu = (1 + L^{\text{corr}}_{\nu\nu'}M^{-1}_{\nu\nu'})S_\nu$ and the weak formulation of the QNE is $L^{\text{pol}}_{\nu\nu'}\delta\phi_{\nu'} = S^{\text{Pade}}_\nu$ where $L^{\text{pol}}_{\nu\nu'}$ is taken from Eq. (17).

D.   Gyroaveraging

For computing gyro-averages appearing in Eqs. (13) and (16), the gyropoints, *i.e.* the particle positions along the gyroring are parametrized by the gyro-angle α

$$\mathbf{x}(\alpha) = \mathbf{X} + \boldsymbol{\rho}(\alpha) = \mathbf{X} + \rho\left(\frac{\nabla s}{|\nabla s|}\cos\alpha + \frac{\mathbf{b}\times\nabla s}{|\mathbf{b}\times\nabla s|}\sin\alpha\right), \tag{21}$$

where $\rho = \rho(\mathbf{X},\mu)$ and having dropped the index σ for species dependence to lighten notation. The $(s,\theta^\star)$ coordinates of the gyropoints can be estimated by linearizing the metric around the guiding-center position. However, such a linearization of the metric is problematic when considering the polar-like coordinate system $(s,\theta^\star)$ which presents a singularity at $s = 0$ (magnetic axis). Indeed, when approaching this point the metric starts to vary significantly over the scale of the Larmor radius. To avoid this problem one considers the pseudo-Cartesian coordinate system $(\xi,\eta) = (s\cos\theta^\star, s\sin\theta^\star)$ which is absent of any singular point. The radial variable s must be defined so as to be proportional to the geometrical minor radius r near the magnetic axis, *e.g.*, $s \propto \sqrt{\psi}$. The estimation of the $(s,\theta^\star)$ coordinates of points along the gyro-ring is now carried out by performing an analytical mapping in between the two sets of variables $(s,\theta^\star) \leftrightarrow (\xi,\eta)$ and by linearizing the metric around the
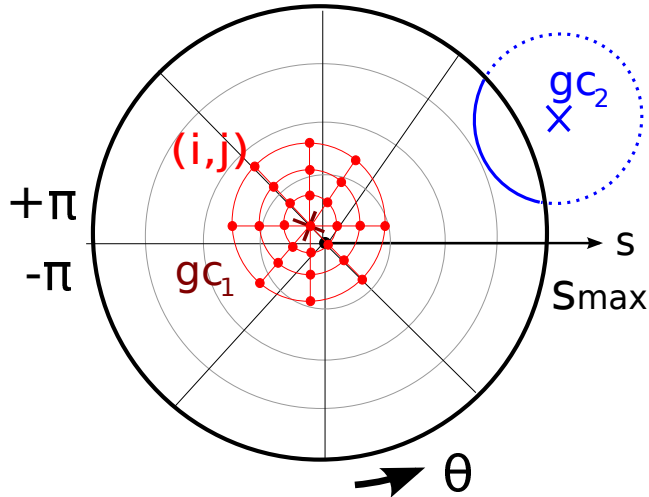
FIG. 1. Sketch of the gyropoints used to compute velocity quadrature of the arbitrary wave-length polarization matrix (A8). In red, plotted is a guiding center gc_1 (dark red cross) located near the magnetic axis (black dot marker) and the local grid of gyropoints (red dot markers), $\{\mathbf{X} + \boldsymbol{\rho}(v_\perp^{(i)}, \alpha^{(j)})\}$, used to compute the local velocity quadrature $(v_\perp^{(i)}, \alpha^{(j)})$ at this guiding center position. In blue, plotted is a guiding-center (gc_2) located outside the simulation domain (blue cross) with its associated gyroring crossing the simulation domain (blue full line).

guiding-center position in the (ξ, η) coordinates, which leads to

$$
\begin{cases}
s(\mathbf{X} + \boldsymbol{\rho}) = \sqrt{s^2(\mathbf{X}) + [\boldsymbol{\rho}(\alpha) \cdot \nabla s(\mathbf{X})]^2 + s^2(\mathbf{X})\,[\boldsymbol{\rho}(\alpha) \cdot \nabla \theta^\star(\mathbf{X})]^2 + 2\,s(\mathbf{X})\,\boldsymbol{\rho}(\alpha) \cdot \nabla s(\mathbf{X})}, \\
\theta^\star(\mathbf{X} + \boldsymbol{\rho}) = \theta^\star(\mathbf{X}) + \arctan\left[\frac{s(\mathbf{X})\,\boldsymbol{\rho}(\alpha) \cdot \nabla \theta^\star(\mathbf{X})}{s(\mathbf{X}) + \boldsymbol{\rho}(\alpha) \cdot \nabla s(\mathbf{X})}\right].
\end{cases}
\tag{22}
$$

E. Quadratures

This section briefly comments numerical requirements for solving the self-consistent electrostatic field when accounting for the ion polarization density at arbitrary wavelength. A focus is made near the axis and near the edge of the simulation domain. Refs. 14 and 15 already discussed the accuracy of the gyroaverage operation for the polarization matrix assembly, in order to resolve short wavelengths.

Near axis, it was found that the grid of gyropoints, $\{\mathbf{X} + \boldsymbol{\rho}_{\mathrm{pol}}(v_\perp^{(i)}, \alpha^{(j)})\}$ see Fig. 1, used for assembling the integral solver must be a few times denser than the radial grid on which the field $\delta\phi$ is represented, in order to avoid non-physical oscillations on $\delta\phi$.
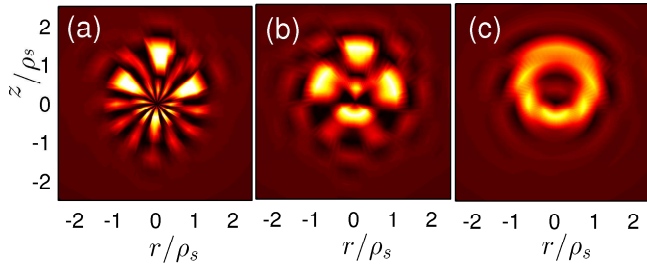
FIG. 2. Electrostatic field, $\delta\phi$, solution to the QNE when the source is a gyroring charge perturbation located such that the magnetic axis, positioned at $(R, Z) = (0, 0)$, is slightly inside the gyroring. Subplot (a) only four points are used to represent the gyroring, (b) four points as well but filtering out the Fourier mode $k_\theta\rho_s > 8$ from the right hand side, and (c) using 100 points to represent the gyroring and no filter. This test case shows the presence of non-physical oscillations near axis caused by the coarse discretization of the gyroaveraging operation when computing the charge assignment.

On the contrary of the long wavelength solver, the arbitrary wavelength solver and the Padé solver are not filtering the short scales. One thus must reduce the short scale sampling error on the source term of the QNE, to avoid the consequent presence of short-scale error on the solved field $\delta\phi$. Therefore, during the charge assignement operation, a Fourier filter (resp. a high number of gyropoints) is used to filter out (resp. to reduce) the pile-up of the error sampling, in particular near axis where the grid resolution is the finest. This error sampling near axis is partly a consequence of the discretness of the gyroaveraging operation, see Fig. 2.

A novelty of the integral operator compared to the differential one concerns the integral operation and its volume of integration. When assembling the integral solver, the quadratures account for guiding centers, $\mathbf{X}$, which are outside the simulation volume if a fraction of their gyroring, $\mathbf{X} + \boldsymbol{\rho}(\alpha)$, is inside this simulation volume. See the guiding-center and gyroring plotted in blue in Fig. 1. This volume of guiding-centers which are outside the simulation domain represents a small volume of a few local thermal Larmor radius in the radial direction, because the quadrature over the perpendicular velocity is typically carried out from 0 to $v_{\perp,max}$ with $v_{\perp,max} = 5v_{\text{th}}$.

The solver matrices implementation is described in the appendix A. Let us just note that when assembling the integral solver with a perpendicular velocity grid which is uniform in

10

$v_\perp$ (resp. μ), the error on the solution converges with the order $\mathcal{O}(\Delta v_\perp^4)$ (resp. $\mathcal{O}(\Delta \mu^2)$).

F.   Boundary conditions

In the integral solver, the electrostatic perturbation field, $\delta\phi$, is only defined within the toroidal simulation domain, *i.e.* there is no $\delta\phi(s)$ for $s < s_{\min}$ or $s > s_{\max}$. Moreover, no boundary condition is applied to the field $\delta\phi$ which is then left free to take edge values consistent with the plasma description. When the domain includes the magnetic axis $s = 0$, one imposes unicity on the solution on axis: $\delta\phi(s = 0, \theta^\star) = \langle\delta\phi\rangle_\theta(s = 0)$ for any $\theta^\star$ as described in Ref. 6. This "unicity boundary condition" on the magnetic axis translates into keeping only the $m = 0$ mode for the field coefficients.

A simple verification of the behavior of $\delta\phi$ on the edge has been carried out in a very simple system of the form $\mathcal{L}\delta\phi = \delta N^{\mathrm{pol}}$ where $\mathcal{L}$ is the integral polarization drift operator (no adiabatic electrons). The background is Maxwellian with constant density and temperatures profiles, the geometry is Cartesian (x, y) x is the "radial" direction and y is the periodic "poloidal" direction, and the perturbation is a pure radial sinusoid $\delta N^{\mathrm{pol}}(x, y) = \sin(k_x x)$ with $k_x = 2p\pi/L_x$, p an integer number, and L_x the simulation width in the x direction. In these conditions, one obtains a theoretical estimate for the field at the edge: $\delta\phi_{\mathrm{theory}} = -(4\rho_{\mathrm{th}}/3\sqrt{2\pi})\partial\delta\phi/\partial x$. In Fig. 3 (a), this theoretical estimate (red full line with cross markers) is in good agreement with the numerical value of the field (thick black line). The agreement is better for long wavelengths because of approximations made for obtaining the analytical relation. Note that the radial derivative $\partial\delta\phi/\partial x$ used for the theoretical estimate is taken from the numerical simulation results. This theoretical estimate is obtained from the following approximation

$$\delta N_{\mathrm{edge}}^{\mathrm{pol}} \simeq -\frac{3}{4}\frac{qN_0}{T_0}\delta\phi + q\frac{\rho_{\mathrm{th}}}{\sqrt{2\pi}}\left[\frac{\delta\phi}{2}\frac{\partial N_0/T_0}{\partial x} - \frac{N_0}{T_0}\frac{\partial\delta\phi}{\partial x}\right]. \tag{23}$$

This relation is obtained by integrating Eq. (16) when gyroaveraging the perturbed field only over the fraction of gyroring which is inside the simulation volume, because the simulated $\delta\phi$ is not defined outside the simulation volume. The Taylor expansion of the gyroaveraging of the perturbation at the edge is thus $\langle\phi\rangle_\alpha \simeq \phi/2 - (\rho/\pi)\partial\phi/\partial x$. The background quantities being defined outside the simulation domain, their gyroaverage Taylor expansion is $\langle N_0\rangle_\alpha \simeq N_0 + (\rho^2/4)(\partial^2 N_0/\partial x^2 + \partial^2 N_0/\partial y^2)$.
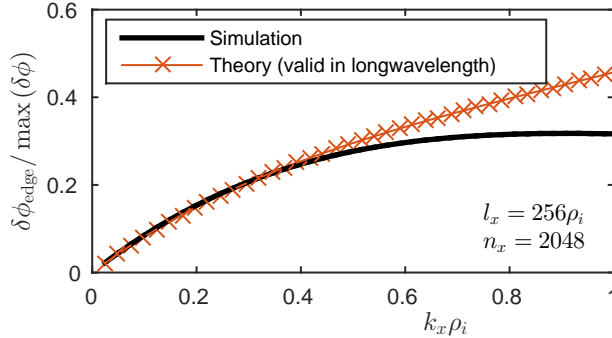
FIG. 3. Value of the electrostatic field at the edge, in a simple test case scenario. Cartesian coordinates, slab geometry, $\delta\phi$ solution to a RHS perturbation $\delta N = \sin(k_x x)$ when solely accounting for the polarization drift operator. The "theory" curve is estimated from equation (23) valid for long wavelengths only (see the text).

G.   Numerical convergence and structure of the polarization matrix

Here we will show that the growth rate of unstable $n \neq 0$ modes can be recovered by using a numerically reduced band matrix for representing the arbitrary wavelength solver matrix[14]. On the other hand, we shall see that one cannot truncate this matrix to accurately simulate the $n = 0$ GAM oscillations and zonal flow residual which are typically studied in a Rosenbluth-Hinton test[25]. Therefore, in view of carrying out nonlinear simulations, one needs to keep the "complete" matrix.

As discussed in Ref. 14, the new arbitrary wavelength polarization matrix has the particularity of being composed of a number of radial bands varying with the splines degree and the $v_{\perp,max}$ parameter. This number of radial bands is given by the relation $n_{\mathrm{rad-bands}} = 2(d+1) + ceil(2\rho_{\max}/\Delta r)$ with $\rho_{\max} = v_{\perp,max}/\Omega_0$ the largest Larmor radius used during the quadrature, and Δr the width of a radial interval Δs in ρ_i units. In our case this radial interval width varies because of the radial profile effects and one should consider the most constraining value of Δr for defining $n_{\mathrm{rad-bands}}$. The total number of radial bands used for representing the arbitrary wavelength solver matrix is thus $n_{\mathrm{bands}} = n_m n_{\mathrm{rad-bands}}$ with n_m the number of discrete Fourier modes used to represent the field in the poloidal direction.

We confirm in a pure TEM case that the eigenvalue of the mode may only be weakly affected by this number of radial bands[14], such that one can truncate the arbitrary wavelength
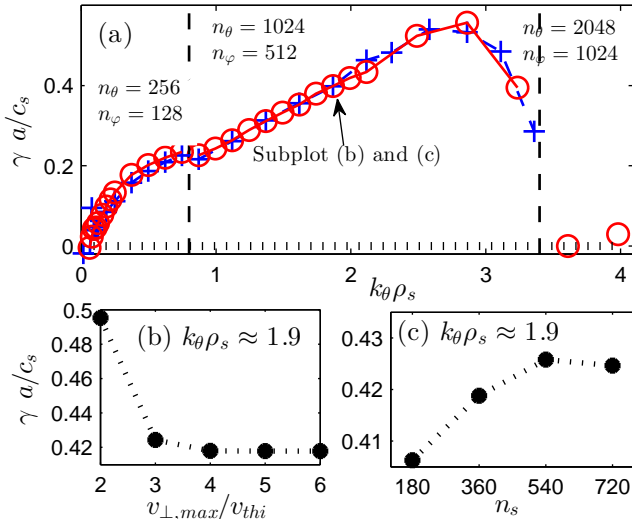
12

FIG. 4. Pure TEM study with hybrid electron model, test case based on CBC but with $L_{T_i} = L_N$, see thesis Ref. 24 for more details on the test case. Radial resolution $n_s = 360$ with $a/\rho_i = 180$. Subplot (a), the polarization matrices used for computing the growth rates are composed of all the twenty seven non-zero radial bands (red) and of only five radial bands (blue). Vertical dashed lines separate three different (n_θ, n_φ) resolution used for this scan. In subplot (b) and (c), convergence studies are carried out with respect to the radial resolution n_s and to the $v_{\perp,max}$ parameter, respectively. In these cases all the non-zero radial bands composing the solver matrix are kept and $v_{\perp,\max} = 5v_{\mathrm{th}}$.

polarization matrix. In Fig. 4 (a), it is shown that keeping only 5 of the 27 matrix radial bands is enough to recover the growth rate of the TEM mode over the whole instability spectra.

In subplots (b) and (c), convergence studies carried out for the toroidal mode number $n = 128$ show that the growth rate is converged with $\Delta r/\rho_i \approx 1/2$ ($n_s = 360$) and $v_{\perp,max} \geq 4v_{\mathrm{th}}$. For the scan carried out in subplot (a), one uses $n_s = 360$ and $v_{\perp,max} = 5v_{\mathrm{th}}$. These parameters are used in the other simulations of this paper (except indicated otherwise).

A Rosenbluth-Hinton test[25] is carried out in Fig. 5. In subplot (a), all the radials bands required for representing the arbitrary wavelength matrix, with $v_{\perp,max} = 5v_{\mathrm{th}}$, are kept and there is a a very good agreement between the results obtained with the long-wavelength solver and the arbitrary wavelength solver. In subplot (b), the relative differences between a theoretical estimate and the simulation results using the arbitrary wavelength solver is
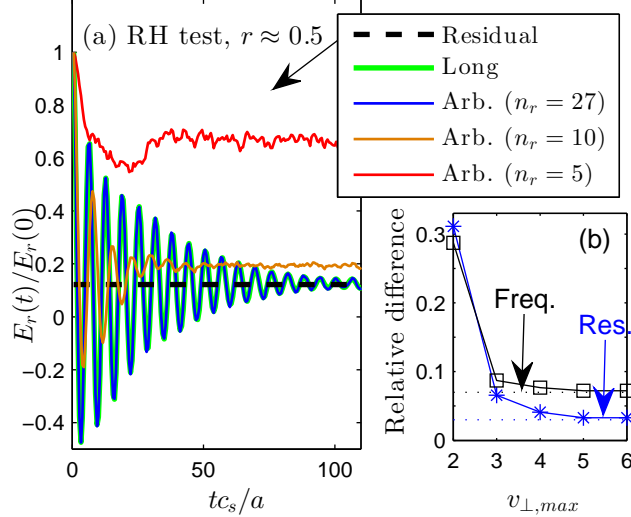
13

FIG. 5. Rosenbluth-Hinton test in CBC geometry with zero density and temperatures gradients, $\rho^\star = 1/180$, $n_s = 360$, $n_{p,\text{tot}} = 16\text{M}$ marker particles, adiabatic electrons, and the results are taken at radial position $r \approx 0.5$. Plotted is the radial electric field E_r in arbitrary units. Subplot (a), comparison between the long and arbitrary wavelength solvers with 27 (blue), 10 (orange), and 5 (red) radial bands fo representing the solver matrix. Subplot (b), convergence study with respect to $v_{\perp,max}$ used for assembling the arbitrary wavelength solver. Plotted are the relative differences of the simulation results with the theoretical estimates: $res = 1/(1 + 1.6 q_s^2 \sqrt{a/R})$ and $\omega_G = (v_{\text{th,i}}/R)\sqrt{1 + 1/2q_s^2}$. The dotted lines, in subplot (b), stand for the long wavelength results.

plotted with respect to the parameter $v_{\perp,\text{max}}$ used for assembling the polarization matrix. For $v_{\perp,max} \geq 5v_{\text{th}}$ the simulation results obtained with both the arbitrary wavelength solver and the long wavelength solver are in good quantitative agreement. In both cases there are reasonable differences of 3% and 7% between the numerical results and the theoretical predictions for the residual $res = 1/(1 + 1.6 q_s^2 \sqrt{a/R})$ and frequency $\omega_G = (v_{\text{th,i}}/R)\sqrt{1 + 1/2q_s^2}$, respectively. In subplot (a), one shows that the results are clearly sensitive to the number of radial bands and that with the arbitrary wavelength solver one clearly needs a larger number of radial bands than with the differential solver, in order to converge the results. These results were numerically converged within a few percent when keeping 80% of the radial bands composing the integral solver matrix. In the simulations presented in the remainder of this paper we will keep all the non-zero radial bands.

III. LINEAR BENCHMARK ORB5 VERSUS GENE

To validate the new solver, a benchmark exercise has been carried out, between ORB5 and the global version of the GENE code[16,17,26], by using realistic magneto-hydrodynamic (MHD) geometries, as well as the different versions of the new ORB5 field solver. For this benchmark exercise, two MHD equilibria from Ref. 27 were used: the geometry V, *MHD-5*, which is the simplest one and the geometry I, *MHD-1*, which is the most complicated one. When using MHD-5, three electron models (adiabatic, hybrid, and kinetic) were used, as well as the three solver versions: long wavelength, Padé, and arbitrary wavelength. When using MHD-1, one used the adiabatic electron model for both the long wavelength and the arbitrary wavelength solvers.

The considered plasma is a two species plasma with ions ($q_i = -q_e = e$), heavy electrons ($m_i/m_e = 400$), and $T_{i0} = T_{e0}$. The background profiles are chosen to be peaked, such as to radially localize the source of instability and to avoid the presence of modes growing with similar growth rates at different radial locations. Both density and temperature profiles are thus defined by

$$\frac{d \ln N, T}{d\rho_{\text{vol}}} = -\frac{\kappa_{N,T}}{2} \left[\tanh \left(\frac{\rho_{\text{vol}} - \rho_{\text{vol},0} + \Delta\rho_{\text{vol}}}{\Delta_{N,T}} \right) - \tanh \left(\frac{\rho_{\text{vol}} - \rho_{\text{vol},0} - \Delta\rho_{\text{vol}}}{\Delta_{N,T}} \right) \right], \quad (24)$$

with $\rho_{\text{vol}} = \sqrt{V/V_{\text{edge}}}$, $V = V(\psi)$ the volume contained within the flux surface ψ, and $\kappa_{N,T} = a/L_{N,T}$. In this benchmark exercise one takes $\kappa_N = 0.78$, $\kappa_T = 2.47$, $\Delta_N = 0.02$, $\Delta_T = 0.02$, $\rho_{\text{vol},0} = 0.5$, and $\Delta\rho_{\text{vol}} = 0.075$ for both ion and electron species.

In Fig. 6, using the fully shaped MHD equilibria MHD-1, the local dispersion relations obtained from simulations carried out with GENE and ORB5 are in good agreement at all wavelengths when using the new arbitrary wavelength solver. It is noticeable that this ITG type mode is unstable down to shorter scales ($0 > k_\theta\rho_i \gtrsim 1.2$) than a typical ITG ($0 > k_\theta\rho_i \gtrsim 0.6$). Thanks to this particularity of the spectra, it is clearly shown that the long-wavelength solver underestimates the growth rate for short wavelength $k_\theta\rho_i > 0.6$.

In Fig. 7, using the simplest MHD equilibria MHD-5, it is shown that the long-wavelength solver totally fails at solving the short wavenumbers of the TEM branch, when using either the hybrid or the fully kinetic electron models. On the contrary, the new arbitrary wavelength solver successfully solves these short scales modes with both the hybrid and drift-kinetic electron models and is in very good quantitative agreement with GENE. Finally, the
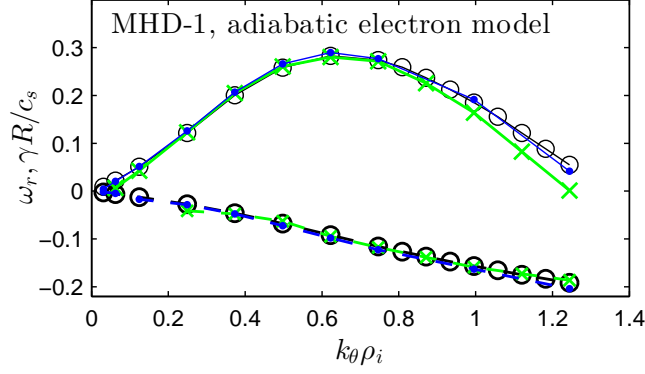
15

FIG. 6. Dispersion relation for the MHD-1 case, results have been obtained with obtained with GENE (black circles), ORB5 and long wavelength solver (green crosses) or arbitrary wavelength solver (blue dots), when using the adiabatic electron model. Growth rate in full line and real frequency in dashed line.
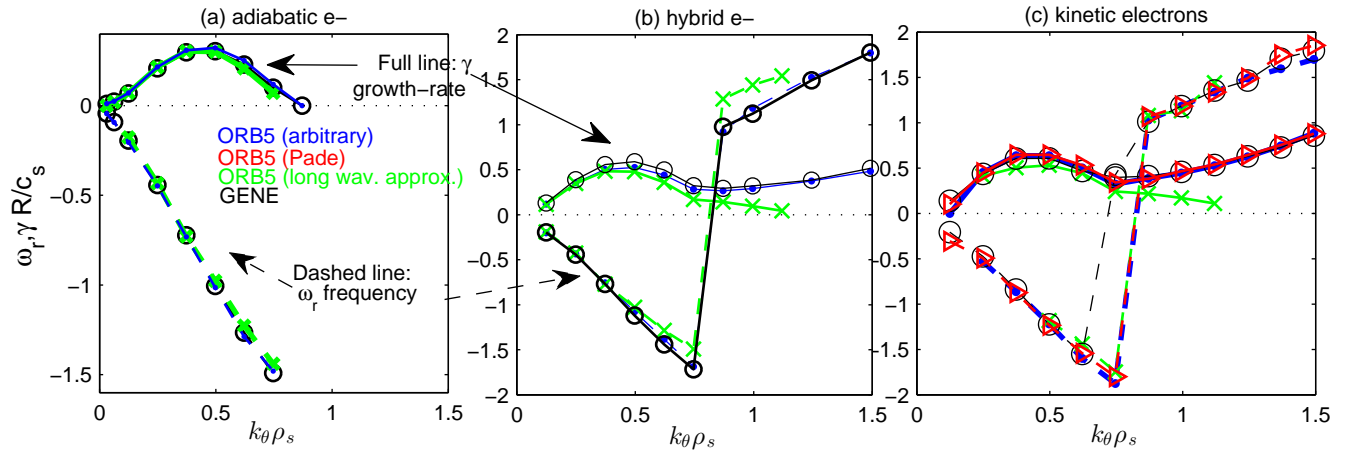
FIG. 7. Dispersion relation for the MHD-5 case, results have been obtained with GENE (black circles), ORB5 and long wavelength solver (green crosses) or Padé approximation solver (red triangles) or arbitrary wavelength solver (blue dots), when using the (a) adiabatic, (b) hybrid, and (c) kinetic electron models. Growth-rate in full-line and real frequency in dashed line.

Padé version of the solver also shows a very good agreement with GENE and thus with the new integral solver.

In Fig. 8 subplots (a) and (b), it is shown that the radial envelopes of the eigenmode $n = 24$ are in very good agreement between GENE and ORB5 when using either the arbitrary wavelength or the Padé solver. Moreover, the systematic presence of fine radial structures

16

due to the non-adiabatic response of passing electrons near MRSs[5] is confirmed, and their width is clearly converged for both ORB5 and GENE (see the zoom). It is remarkable that the Padé approximation version of the solver is still valid for such short scale $\delta r \approx 0.3\rho_i$ corresponding roughly to $k_r\rho_i \approx 20$. It is also remarkable that there is such a good agreement when using the drift-kinetic model for the electron (ORB5) and the gyro-kinetic model for the electron (GENE). On the other hand, it is shown that the long wavelength solver fails at solving these fine radial structures. Note that fine structures of similar short scales are present on the source term of the quasi-neutrality equation, $\delta N_i^{\mathrm{gy}} - \delta N_e^{\mathrm{gy}}$, when using either the long or arbitrary wavelength solver, see subplot (c). It clearly shows that the absence of fine structures on the potential envelope is only a consequence of the long wavelength approximation used.

For the results obtained when using the arbitrary wavelength solver, the fact that the growth rate is larger when using the fully-kinetic electron model than when using the hybrid electron model shows that the non-adiabatic passing electron response is not only corrugating the eigenmode radial structure but furthermore enforces the destabilization mechanisms. For example (see Fig. 7) for the wave number $k_\theta\rho_s \approx 1.2$ of the TEM branch, the growth rate is $\gamma \simeq 0.38$ with the hybrid electron model and $\gamma \approx 0.64$ with the fully kinetic electron model.

IV.   TCV SIMULATIONS

In this section, we present global nonlinear simulations of a two species plasma, *i.e.*, kinetic ions and electrons, carried out in conditions relevant for TCV shot #45353. The magnetic geometry is shaped with elongation, triangularity, and Shafranov shift, see Fig. 9. This TCV shot was initially used in Ref. 24 where nonlinear simulations were carried out with ORB5 using a simpler model for the plasma, *i.e.* the hybrid electron model, the long-wavelength solver, and a lower radial resolution ($n_s = 128$), thus missing the physics of passing electrons near MRSs.

In this section, we start to compare results of a half torus simulations carried out with the Padé solver and with the arbitrary solver. We then compare results of these half torus simulations with a full torus simulation. Finally we compare the simulation results of the half torus test case carried out with the heavy electron mass ratio $m_i/m_e = 400$ with the same

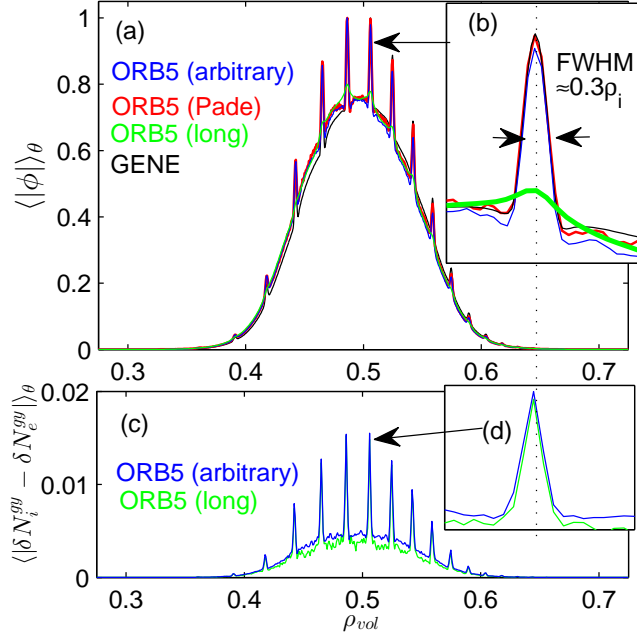FIG. 8. Eigenmode radial structure (poloidal-average without the Jacobian) of the electrostatic field in subplots (a,b), and of the guiding-center charge density in subplots (c,d). Results have been obtained with GENE (black), ORB5 with long wavelength solver (green), ORB5 with arbitrary wavelength solver (blue), and ORB5 with Padé approximation solver (red). Toroidal mode number $n = 24$ in the ITG regime. One uses a very high radial resolution: 800 (1000 for GENE) radial points on the plotted radial interval.

simulation carried out with the physical deuterium to electron mass ratio $m_i/m_e = 3672$.

A.   Test case description

The *half-torus* case is carried out by using the toroidal mode spectrum $n \in [0, 2, 4, \cdots, 42, 44]$ with $n_{p,tot} = 10^9$ marker particles for each ion and electron species. The *full-torus* case is carried out by using the toroidal mode spectrum $n \in [0, 1, 2, \cdots, 43, 44]$ and keeping the same number of marker particles per toroidal mode number.

The configuration space grid resolution is $n_s \times n_\theta \times n_\varphi = 360 \times 1024 \times 512$ with $s \in [0.35, 1.0]$ and $\rho^\star = \rho_s/a = 1/81$ at the position of reference $s_{peak} = 0.6$ ($\rho_{vol} \approx 0.48$). The temperature ratio being equal to $T_{i0}/T_{e0} = 0.2667$, TCV is a "big" machine for the ions with $\rho_i/a \approx 1/157$ at s_{peak} and the chosen radial simulation domain represents more than 100 ion Larmor radii. According to Ref. 5, this grid configuration, with several points per
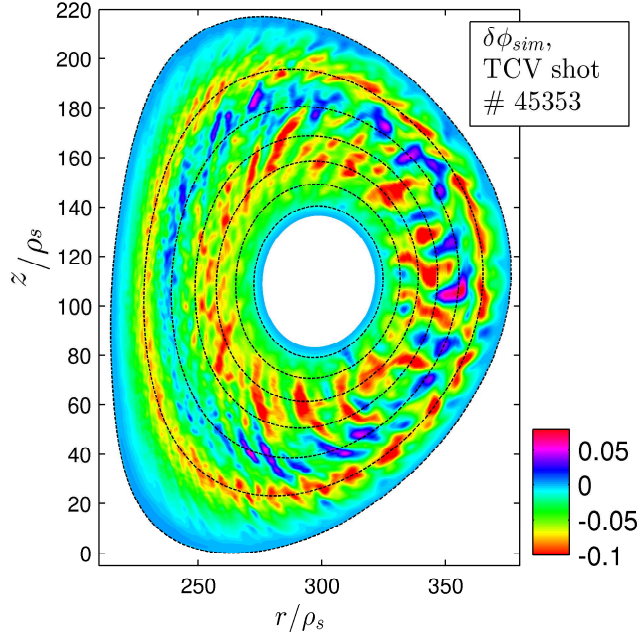
FIG. 9. Electrostatic field in the poloidal plane, snapshot taken during the turbulent saturated time window. TCV full-torus simulation test case.

ion thermal Larmor radius, should be large enough for resolving the fine radial structures.

A typical field aligned filter[7,10] is used such that for a given toroidal mode number n only the poloidal modes contained in the local interval $m \in [nq_s - 5, nq_s + 5]$ are solved.

A modified Krook operator[9] is used for controlling the noise by setting the parameter $\gamma_k a/c_s = 0.027$ (heavy electrons) and 0.024 (Deuterium/electron mass ratio) which roughly corresponds to a tenth of the respective maximum linear growth rates. This operator does not introduce sources of particles or parallel momentum and conserves the residual ZFs phase space structure. The Krook operator is used to keep the species temperature profiles close to their initial values. The associated heat source is a smooth radial function corresponding consistently to a source near the core and a sink near the edge. The radial density profile can relax during the simulation and the time-averaged (over the turbulent saturated regime) profile shows a significant deviation from the initial input, by up to $10 - 20\%$. This loss of density is caused by a strong burst of particle flux when the system state enters in the nonlinear saturated regime, after which there is a remaining particle flux of decreasing amplitude during the simulation so that the density continues to relax. This relaxation of the density profile is currently not taken into account by the assembly of the solver. Doing that would require implementing the nonlinear polarization drift contribution to the QNE, which

19

is left for future works. Shielding of electric field[23] is used at the edges of the simulation domain, to avoid the presence of non-physical electric field caused by secular accumulation of charge losses near the boundary.

B. ORB5 moments and fluxes diagnostics

A new 3D diagnostic feature is implemented in the ORB5 code. In these new diagnostics, the moments of the particle perturbation distribution function, δf, are computed by doing a Galerkin projection of the marker weights, which are furthermore weighted by 1 for density and $mv^2/2$ for kinetic energy, on the same DFT-finite-element representation as the one used for the perturbed electrostatic potential $\delta\phi$. In addition, this projected quantity is multiplied by the inverse mass matrix such as to obtain the DFT-finite-element coefficients of the expected physical quantity. The computation of these moments is comparable to the coefficients of the source term in Eq. (19). For example, the DFT finite-element coefficients of the perturbation density are computed from

$$(\delta N_{\sigma,g})_{k'} = \mathcal{M}_{kk'}^{-1} \sum_p w_p \, 1 \, \left(|\tilde{E}_g \leq \tilde{E}_p < \tilde{E}_{g+1}| \times |\lambda_g \leq \lambda_p < \lambda_{g+1}|\right) \, \langle\hat{\Lambda}_k\rangle_\alpha(\mathbf{X}_p, \mu_p), \quad (25)$$

where the perturbation moment is furthermore split in velocity space subgroups labeled g, and the value of an inequality is one or zero. These subgroups are flexibly determined by any 2D grid over the normalized kinetic energy $\tilde{E} = E_{\rm kin}/T_\sigma(\mathbf{X})$ and the signed pitch angle $\tilde{\lambda} = sign(v_\parallel)\lambda/\lambda_c$ with $\lambda = |\arctan v_\perp/v_\parallel|$ and $\lambda_c = \arccos\alpha_{\rm trap}(\mathbf{X})$. These new diagnostics are also used in the following sections for computing the electron particle flux spectra.

In ORB5, the gyrocenter fluxes are computed from equation[24]

$$\bar{\mathcal{F}}_\sigma[\mathcal{A}] = \left\langle \frac{\nabla\psi}{|\nabla\psi|} \cdot 2\pi \int_0^{+\infty} d\mu \int_{-\infty}^{+\infty} dv_\parallel \frac{B_{0\parallel}^\star}{m_\sigma} \mathcal{A} \, f_\sigma \dot{\mathbf{X}} \right\rangle_\mathcal{S}, \quad (26)$$

where $\dot{\mathbf{X}}$ is the guiding-center drift and $\mathcal{A}$ is a function of position and velocity $\mathcal{A} = \mathcal{A}(\mathbf{X}, \mu, v_\parallel)$ such that the particle, kinetic energy, potential energy, and heat fluxes are then, respectively, defined by $\bar{\Gamma}_\sigma = \bar{\mathcal{F}}_\sigma[1]$, $\bar{Q}_{{\rm kin},\sigma} = \bar{\mathcal{F}}_\sigma[mv^2/2]$, $\bar{Q}_{{\rm pot},\sigma} = \bar{\mathcal{F}}_\sigma[q\phi]$, $\bar{q}_{{\rm h},\sigma} = \bar{\mathcal{F}}_\sigma[m(v^2 - 5v_{{\rm th},\sigma}^2)/2 + q\phi] = \bar{Q}_{{\rm kin},\sigma} + \bar{Q}_{{\rm pot},\sigma} - (5/2)T_\sigma\Gamma_\sigma$. In Eq. (26), the brackets $\langle\ \rangle_\mathcal{S}$ denote the surface average

$$\langle\mathcal{A}\rangle_\mathcal{S}(\psi, t) = \frac{1}{\int_{\mathcal{S}(\psi)} d\mathcal{S}} \int_{\mathcal{S}(\psi)} d\mathcal{S}\mathcal{A},$$

with $dS = d\varphi d\theta^\star \mathcal{J}|\nabla\psi|$ and $\int_{\mathcal{S}(\psi)} dS \mathcal{A} = \oint d\varphi \oint d\theta^\star \mathcal{J}(\psi, \theta)|\nabla\psi(\psi, \theta^\star)|\mathcal{A}(\psi, \theta^\star)$. In term of the flux-surface average operation, the surface average reads $\langle\mathcal{A}\rangle_{\mathcal{S}} = \langle|\nabla\psi|\mathcal{A}\rangle_{FS}/\langle|\nabla\psi|\rangle_{FS}$. Numerically the flux-surface averaged quantities are computed from the approximation

$$\langle\mathcal{A}\rangle_{FS} \simeq \langle\mathcal{A}\rangle_{\Delta V} = \frac{1}{\Delta V}\int_{\Delta v} d^3 V \mathcal{A},$$

with ΔV the volume delimited by the surfaces ψ and $\psi + \Delta\psi$. This approximation is exact in the limit of $\Delta\psi \to 0$.

For electrons, the gyrocenter fluxes match the particle fluxes because $\boldsymbol{\rho}_e \simeq 0$. For ions, $\boldsymbol{\rho}_i \neq 0$ and one needs to account for the polarization and magnetization correction terms[28,29] such that one has the relation

$$\boldsymbol{\Gamma}_\sigma = \bar{\boldsymbol{\Gamma}}_\sigma + \partial\mathbf{P}_\sigma/\partial t + \nabla \times \mathbf{M}_\sigma,$$

where $\partial\mathbf{P}_\sigma/\partial t$ is a polarization current contribution to the particle flux and $\nabla \times \mathbf{M}_\sigma$ is a magnetization current contribution to the particle flux[28,29]. In a quasi-steady state, the surface- and time-averaged fluxes of particle and gyrocenters are essentially equivalent $\langle\Gamma_\sigma\rangle_t(s) = \langle\langle\boldsymbol{\Gamma}_\sigma\rangle_{\mathcal{S}}\rangle_t \simeq \langle\langle\bar{\boldsymbol{\Gamma}}_\sigma\rangle_{\mathcal{S}}\rangle_t$. The magnetization current contribution goes to zero when averaging over a closed toroidal surface. From now on, no more distinction will be made between the gyrocenter fluxes and the particle fluxes except if relevant for the discussion.

The particle diffusivity and the heat diffusivity are defined by

$$D_\sigma = \Gamma_\sigma / \left\langle -\frac{\nabla\psi}{|\nabla\psi|} \cdot \nabla N_\sigma \right\rangle_{\mathcal{S}} \simeq \frac{\Gamma_\sigma \langle|\nabla\psi|\rangle_{FS}}{(-dN_\sigma/d\psi)\langle|\nabla\psi|^2\rangle_{FS}}, \tag{27}$$

and

$$\chi_\sigma = q_{\sigma,H} / \left\langle -\frac{\nabla\psi}{|\nabla\psi|} \cdot N_\sigma\nabla T_\sigma \right\rangle_{\mathcal{S}} \simeq \frac{q_{h,\sigma} \langle|\nabla\psi|\rangle_{FS}}{N_\sigma(-dT_\sigma/d\psi)\langle|\nabla\psi|^2\rangle_{FS}}, \tag{28}$$

where one assumes that $N = N(\psi)$ and $T = T(\psi)$. These quantities are expressed in gyro-Bohm units $D_{GB} = \chi_{GB} = \rho_{s0}^2 c_{s0}/a$ with $c_{s0} = \sqrt{T_{e0}(s = 0.6)/m_i}$ and $\rho_{s0} = mc_{s0}/qB_{\text{axis}}$.

C. Arbitrary wavelength and Padé solvers in the *half-torus* test case with heavy electrons

The time-dependent radial profile of particle flux, $\Gamma(\rho_{vol}, t)$, electron heat flux, $q_{H,e}(\rho_{vol}, t)$, and electron heat diffusivity, $\chi_e(\rho_{vol}, t)$, are plotted in Fig. 10. The simulation time window
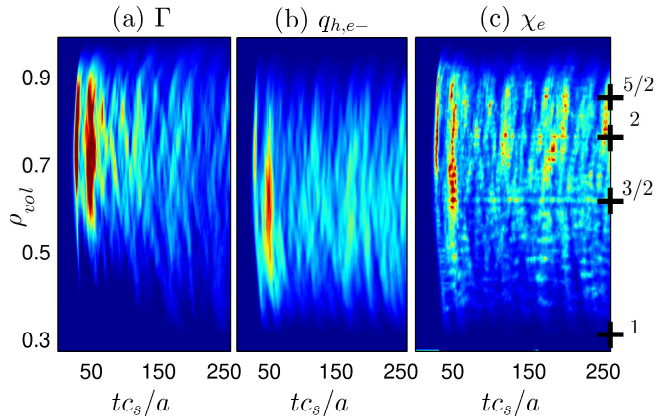
FIG. 10. Particle flux (a), electron heat flux (b), and electron heat diffusivity (c) with respect to the time, tc_s/a, and radial position, $\rho_{\rm vol}$. Global simulation of TCV #45353 using the arbitrary wavelength solver, the kinetic electrons, the heavy electron mass ratio $m_i/m_e = 400$, in a half torus.

covers several flux bursts during the turbulent saturated regime, thus ensuring a reasonably good enough statistics. Fig. 11 subplots (a) and (b) show the radial profile of the time-averaged heat diffusivity of the ions $\langle \chi_i \rangle_t(s)$ and electrons $\langle \chi_e \rangle_t(s)$, respectively. For simulations carried out with both the Padé solver and the arbitrary wavelength solver, the time-averaged ion heat diffusivity is more pronounced near the core and the time-averaged electron heat diffusivity is more pronounced near the edge, as expected from ITG and TEM regimes, respectively. Each species heat diffusivity is found to be in good quantitative agreement between simulations carried out with either the Padé solver or the arbitrary solver. There is only 6% of relative difference between their time- and radial-averaged amplitudes, see the dotted lines in Fig. 11. Moreover, $\langle \chi_i \rangle_t$ and $\langle \chi_e \rangle_t$ are of similar level, but having a constant temperature ratio $T_{e0}/T_{i0} = \nabla T_{e0}/\nabla T_{i0} \simeq 3.75$ the total heat flux, roughly $q_h \simeq \langle \chi_i \rangle_t N |\nabla T_{i0}| + \langle \chi_e \rangle_t N |\nabla T_{e0}|$, is essentially dominated by the electron contribution.

In simulations carried out with either the arbitrary solver or the Padé solver, both the time-dependent and time-averaged radial profiles of electron heat diffusivity, respectively plotted in Figs. 10(c) and 11(b), show the systematic presence of fine radial structures near MRSs which are due to the nonadiabatic response of passing electrons[5]. These corrugations are clearly more pronounced at the surfaces of safety factor $q_s = 3/2, 2, 5/2$ compared to other rational surfaces, because these rational surfaces are of lowest order in the case of a half-torus simulation. The electron heat flux, $q_{h,e}$, being smooth in the radial direction,
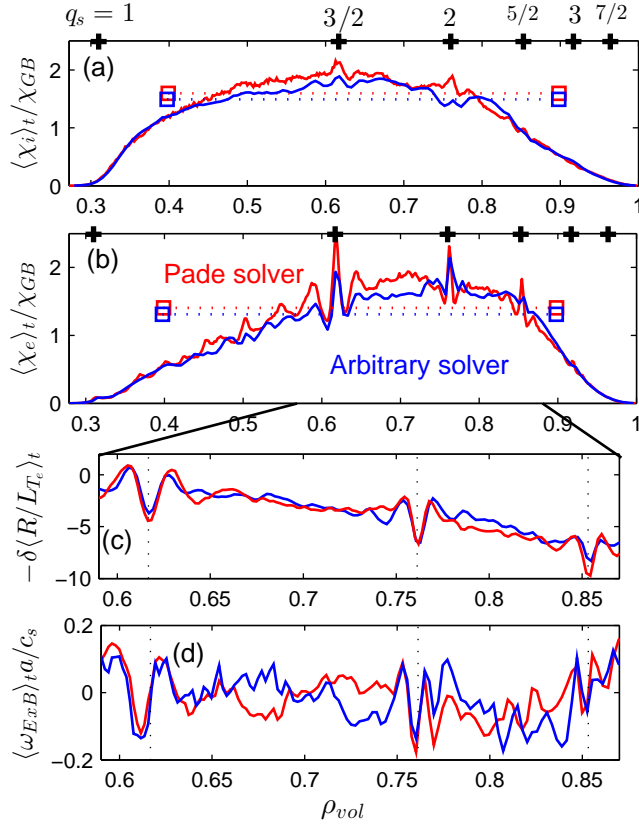
FIG. 11. Time-averaged radial profile of the heat diffusivity of (a) the ions and (b) the electrons, for the simulation of Fig. 10. Radial profiles of (c) the time-averaged electron temperature gradient perturbation and (d) the time-averaged $E \times B$ shearing rate. Padé solver (red) and arbitrary wavelength solver (black) test cases. Time averaged quantities, $\langle \cdot \rangle_t$, are obtained over the turbulent saturated regime for $tc_s/a > 75$. A shorter time-window is used for the full-torus.

see Fig. 10(b), the presence on $\chi_e \propto q_{h,e}/\nabla T_e$ of these fine radial structures near MRSs is the result of the presence of similar fine structures on $\langle \delta R/L_{T_e} \rangle_t$. It should be pointed that the $E \times B$ ZF shearing rate, Fig. 11(d), is zero at lowest order MRSs where the electron temperature gradient perturbation has a local maximum, more comments will be made in Sec. IV E 5. We have checked, by varying the value of the Krook parameter, that the observed corrugations are not due to an artefct of the Krook operator. A similar analysis was shown in Ref. 30.

The time-dependent radial profile of the $E \times B$ ZF shearing rate is plotted in Fig. 12 and
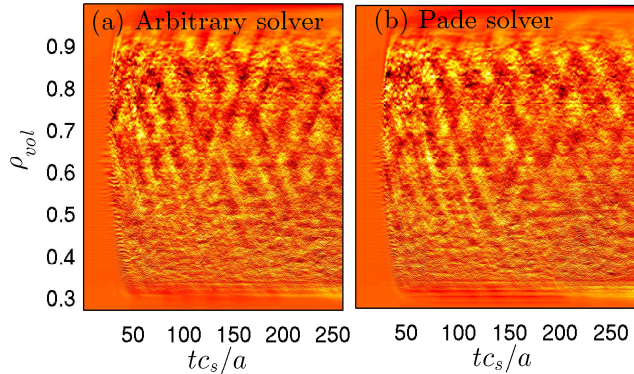
FIG. 12. $E \times B$ ZF shearing rate with respect to the time and to the radial position. Subplot (a) arbitrary solver, (b) Padé solver. For the parameters of Fig. 10.

is computed with equation

$$\omega_{E \times B} = \frac{s}{2\psi q}\frac{d}{ds}\left(\frac{1}{s}\frac{d\langle\delta\phi\rangle_{FS}}{ds}\right), \tag{29}$$

see Refs. 31 and 32. This field is computed from the finite-element representation of $\delta\phi$ and thus provide an insight on the numerical resolution which is achieved by the field solver. The $E \times B$ ZF shearing rate being essentially a second order radial derivative of the electrostatic field, the short scales noise is much more visible than on the potential $\delta\phi$. It is of interest to observe that, in both simulations carried out with the Padé solver and with the arbitrary wavelength solver, the $E \times B$ ZF shearing rate has the same level of noise. It shows that the numerical approximations made for assembling the arbitrary wavelength solver, in particular the polarization drift integral form, are not responsible for the presence of significant short scale errors. Notice that the low level of noise reached in these simulations is possible because of the use of a high number of particles (10^9) and of a high number of gyropoints (18 for thermal ion Larmor radius) for computing the RHS of the QNE.

Fig. 13 shows the time-dependent radial-averaged amplitude of the $E \times B$ ZF shearing rate $\langle|\omega_{E \times B}|\rangle_s(t)$ in subplot (a), and the time-window averaged $E \times B$ shearing rate, $\omega_{eff}(t_w) = \langle|\langle\omega_{E \times B}\rangle_{t_w}|\rangle_{st}$, in subplot (b), which is given by

$$\omega_{eff}(t_w) = \int_{s_{\min}}^{s_{\max}} \frac{ds}{s_{\min} - s_{\max}} \int_{t_1}^{t_{\mathrm{end}}} \frac{dt}{t_{\mathrm{end}} - t_1}\left|\int_t^{t+t_w}\frac{dt'}{t_w}\omega_{E \times B}(s,t')\right|, \tag{30}$$

with $t_1 = 75a/c_s$ in our case, see Ref. 5 for more details. It is clearly shown in subplot (b) of Fig. 13 that the Padé solver and the arbitrary wavelength solver have the same ω_{eff} at all t_{w} and thus the same temporal spectra for $\omega_{E \times B}$.
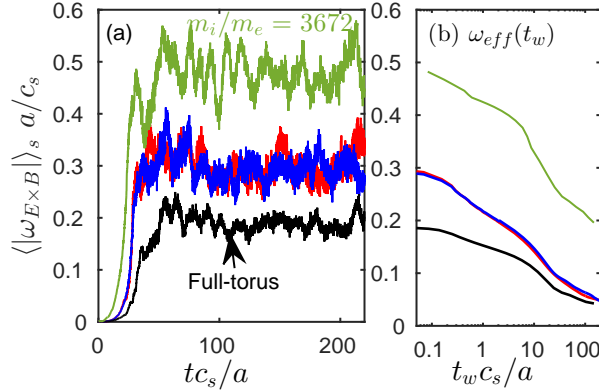
24

FIG. 13. Radially averaged (a) $E \times B$ ZF shearing rate versus time and (b) time-windowed averaged $E \times B$ shearing rate versus size of the window t_w, $\omega_{eff}(t_w) = \langle |\langle \omega_{E \times B} \rangle_{t_w}| \rangle_{st}$, see Eq. (30). Color code: blue for the half-torus case with arbitrary solver and heavy e-, red for the half-torus case with Padé solver and heavy e-, black for the full-torus with arbitrary solver and heavy e-, green for the half-torus with arbitrary wavelength solver and real electron mass ($m_i/m_e = 3672$).

D. Full-torus versus half-torus simulations

Fig. 14 compares results of the previous half-torus simulation with a full-torus simulation carried out with heavy electrons, as well. This figure shows the radial profiles of the time-averaged ion heat diffusivity (a), the time-averaged electron heat diffusivity (b), the electron temperature gradient perturbation (c), and the $E \times B$ ZF shearing rate (d). The major difference between these radial profiles obtained in the half-torus and full-torus cases is the presence, in the half-torus test case, of non-physical fine structures of big amplitude near non integer rational surfaces, see Figs 14 near $q_s = 3/2$ for example. In a realistic full-torus simulation, all the required toroidal mode numbers n are accounted for, and solely the magnetic surfaces of integer safety factor, $q_s = m/1$ with m an integer, are of lowest order. As a consequence, the magnetic surfaces of rational safety factor $q_s = p + 1/2$ with p an integer are, in reality, not of lowest order. Only the mode of toroidal numbers $n = 2p'$ (half of the spectra) can be exactly field aligned at these surfaces where there exist p' and m' integers such that $q_s = p + 1/2 = m'/2p'$. By carrying out a half-torus simulation, one artificially increases the fraction of simulated modes to which the passing electron respond nonadiabatically. For example, in Fig. 14 (b), the fine structures at the magnetic surfaces of safety factor $q_s = 3/2$ and $5/2$ have almost disappeared from the full-torus simulation
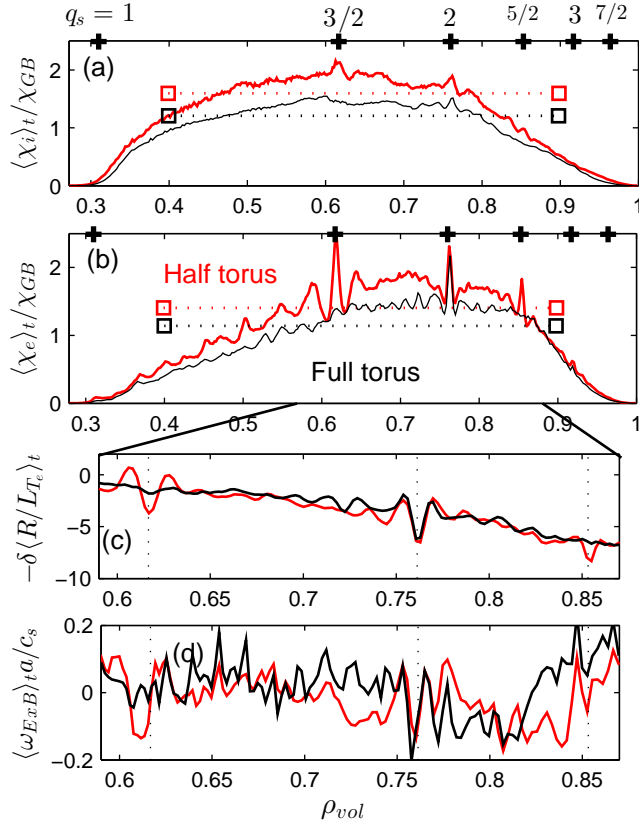
25

FIG. 14. Time-averaged radial profile of (a) the heat diffusivity of the electrons, (b) electron temperature gradient perturbation, and (c) $E \times B$ ZF shearing rate. Half-torus (red) and full-torus (black) test cases with heavy electrons.

results. This is also clearly visible on the electron temperature gradient perturbation, see subplot (c). Realistic nonlinear simulations including the physics of kinetic electrons must then contain the whole toroidal mode spectrum, in order to properly simulate the physics of kinetic electrons near MRSs.

The radially averaged $E \times B$ shearing rate, $\langle |\omega_{E \times B}| \rangle_s$, is decreased by 34% in the full-torus case compared to the half-torus case, see Fig. 13(a). This decrease of the $E \times B$ shearing occurs at all fluctuation time scales, see Fig. 13(b). We also observe a 24% and 19% relative decrease of, respectively, the ion and the electron heat diffusivity in the full-torus simulation compared to the half-torus case. This observation is not in contradiction with the ZF saturation mechanism paradigm: we actually use a different number of toroidal mode numbers for these two simulations, and this affects not only the $E \times B$ shearing rate but the whole turbulence spectrum organization and energy density. Another remark is

that the corrugations of the time-averaged $E \times B$ ZF shearing rate are almost drown in the fluctuations, see Fig. 14, whereas in the flux tube simulation of Ref. 5 these long time-averaged fine structures were of the same amplitude as the fluctuations. We shall see in Sec. IV E 5 that this low level of corrugations on the time-averaged $\omega_{E \times B}$ is essentially due to the choice of using heavy electrons for this test case.

E.   Half torus simulation with the physical Deuterium to electron mass ratio

In this section, we present the results of a fully kinetic simulation carried out with the Deuterium to electron mass ratio $m_i/m_e = 3672$. In this case, the annular width has been slightly reduced in order to decrease the numerical cost of the simulation. It is a half torus simulation with $s \in [0.5, 1.0]$ and $n_s = 360$, $n \in [0, 2, 4, \cdots, 42, 44]$. The Krook parameter is set to $\gamma_k a/c_s = 0.027$ to match 10% of the linear growth-rate.

We also re-run a nonlinear simulation with $m_i/m_e = 400$ when using the same numerical resolution. The only exception being the Krook parameter which is set at $\gamma_k a/c_s = 0.024$ again to match 10% of the linear growth-rate. In Fig. 15, the simulation carried out with $m_i/m_e = 400$ clearly has higher transport levels associated to lower gradient drives, compared to the simulation carried out with $m_i/m_e = 3672$. Prior to discuss this reduction of the turbulence, the linear regime is studied in more details so as to give more insight on the unstable nature of this configuration.

1.   Linear destabilization

In a tokamak, the destabilization mechanisms are, not only but at least in the regimes we study, related to the drift motion of particles which can act as a source or sink of energy for the field. In the electrostatic plasma of interest, the field energy is defined by[6,7]

$$\mathcal{E}_{\text{field}} := (q_i/2) \int d\mathbf{x} \delta N^{\text{pol}}(\mathbf{x}) \delta \phi(\mathbf{x}),$$

and the kinetic energy of the plasma is defined by

$$\mathcal{E}_{\text{kin}} := \sum_{\sigma} \int d\mathbf{X} dv_{\parallel} d\mu d\alpha \frac{B^*_{0\parallel}}{m_{\sigma}} f_{\sigma} \left(\mu B_0 + \frac{m_{\sigma}}{2} v_{\parallel}^2 \right).$$

In a closed system, the conservation of energy, which is only possible in a nonlinear simulation without dissipation, sources, or sinks, imposes $d\mathcal{E}_{\text{tot}}/dt = d(\mathcal{E}_{\text{kin}} + \mathcal{E}_{\text{field}})/dt = 0$.
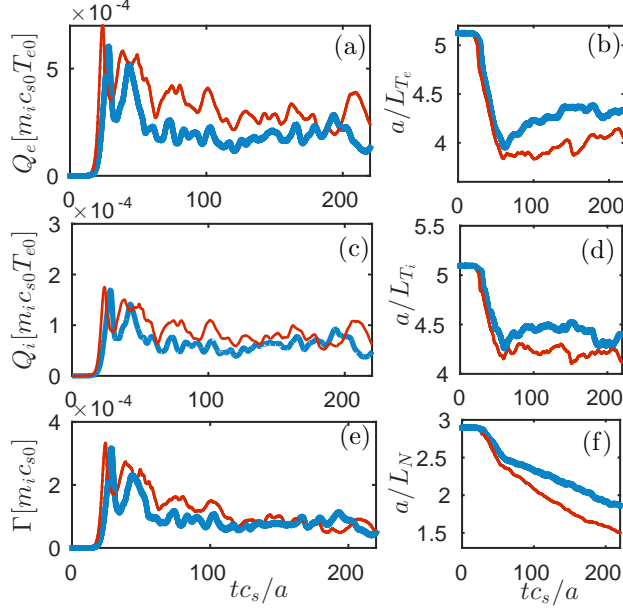
FIG. 15. Nonlinear simulation results of TCV carried out with heavy electrons (red) and physical D/e^- mass ratio (blue thick line). Radial transport of (a) electron heat flux, (c) ion heat, and (e) particle. Radial averaged inverse gradient lengths of the (b) electron temperature profile, (d) ion temperature profile, and (f) of the particle density. Results show a higher level of transport associated to a lower gradient when using the heavy electrons $m_i/m_e = 400$ instead of the D/e^- mass ratio $m_i/m_e = 3672$. The density profile continuously relax because no particle source is considered in these nonlinear simulations.

In a linear simulation this is not possible but one can nonetheless verify the consistency of the power transfer, as introduced in Refs. 13 and 33. This consistency can be verified by comparing the growth rates computed either from the field energy or from the kinetic energy. These growth rates are, respectively, given by the equations

$$\gamma_{\text{field}} = \frac{1}{2\mathcal{E}_{\text{field}}} \frac{d\mathcal{E}_{\text{field}}}{dt},$$

and

$$\gamma_{\text{kin}} = -\frac{1}{2\mathcal{E}_{\text{field}}} \sum_\sigma q_\sigma \int d\mathbf{X} d\mathbf{v} \, \delta f_\sigma \, \dot{\mathbf{X}} \cdot \langle \mathbf{E} \rangle_\alpha, \tag{31}$$

where the approximation $-\nabla \langle \phi \rangle_\alpha \simeq \langle \mathbf{E} \rangle_\alpha$ is made, and the equality $d\mathcal{E}_{\text{field}}/dt = -d\mathcal{E}_{\text{kin}}/dt = q_i \int d\mathbf{X} d\mathbf{v} \, f_i \, \dot{\mathbf{X}} \cdot \langle \mathbf{E} \rangle_\alpha$ has been employed. In ORB5, the kinetic growth rate $\gamma_{\text{kin}} = \gamma_\parallel + \gamma_{\nabla B} + \gamma_{\text{curv}} + \gamma_{\nabla P}$, which is computed from the total drift $\dot{\mathbf{X}} = v_\parallel \mathbf{b} + \mathbf{v}_{\nabla B} + \mathbf{v}_{\text{curv}} + v_{\nabla P}$, is furthermore split in between the different drift contributions: $v_\parallel$ the parallel drift, $v_{\nabla B}$
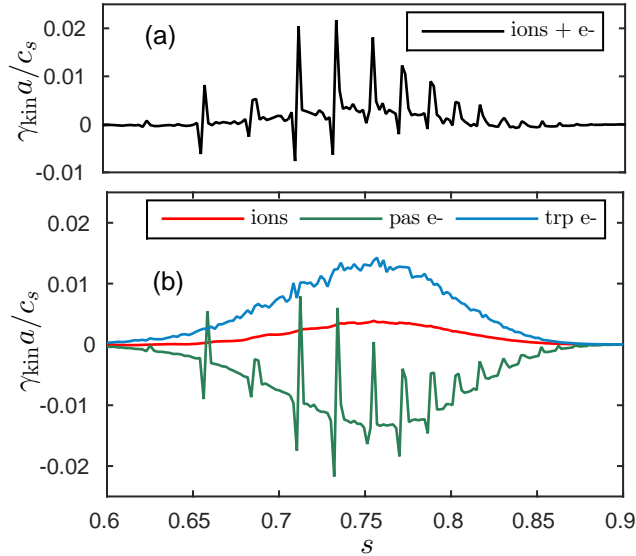
FIG. 16. Radial contribution from the different species to the kinetic growth rate γ_{kin}. Linear simulation, TCV test case, $n = 16$ mode, $m_i/m_e = 3672$. Subplot (a) all species, subplot (b) the contribution of the ions, passing electrons, and trapped electrons are decomposed. This quantity is not computed from the particles motion so that some reduced polarization terms are missing to fully appreciate the ion radial organization.

the "grad B" drift, v_{curv} the curvature drift, and $v_{\nabla P}$ the pressure gradient drift (of small amplitude in our case). See Ref. 7 for the definition of these drifts.

Numerically, the field is represented with finite elements, and the particle phase space is represented with marker particles by using a PIC representation[6,7]. As a consequence, simulations must be carried out with a high enough radial resolution and a high enough number of particles to properly simulate the particle-field interactions, because fine radial structures are present on both the electrostatic field and on the perturbation density. To converge the numerical estimate of γ_{kin}, in simulations carried out with $m_i/m_e = 3672$, it appeared that it was necessary to use a higher radial resolution, when keeping a constant density of markers per radial interval, than in simulations carried out with $m_i/m_e = 400$, in order to converge γ_{kin} with γ_{field}. Indeed in Fig. 16, the contributions to γ_{kin} from the different groups of particles are plotted with respect to the radial position s. One can clearly appreciate that the particle-field interaction is finely corrugated near MRSs so that one needs a good enough resolution for converging this local contribution to the destabilization.

In this TCV test case, the plasma is destabilized by a mixed ion temperature gradient
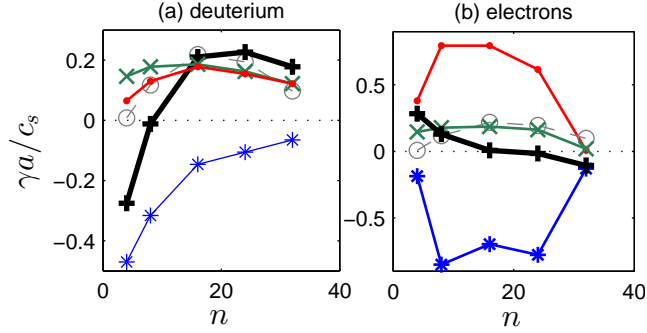
FIG. 17. Species contribution to the linear growth rate $\gamma_{\rm kin}$ (black +), Eq. (31), is decomposed into the drift contributions $\gamma_\parallel$ (blue *), $\gamma_{\nabla B}$ (red •), $\gamma_{\rm curv}$ (green ×). Note that the overall growth rate $\gamma = \gamma_i + \gamma_e$ is plotted with gray dashed lines and circle markers in both subplots.

(ITG) and trapped electron mode (TEM) regime. The instability is driven by the electrons at low n and by the ions at higher n, up to $n \simeq 32$ which corresponds roughly to $k_\perp \rho_i \simeq 0.6$ or $k_\theta \rho_s \simeq 1.2$. The species contributions to the destabilization are split into their different drift contributions in Fig. 17. In the electron case, the parallel damping is essentially due to the passing electrons and the grad-B and curvature drift destabilizing influence is essentially due to the trapped electrons. In the ion case, the passing and trapped particles are both contributing to the different drift terms in a more complex manner. Finally, the nonlinear simulations are carried out up to $n = 44$ which corresponds to $k_\theta \rho_i \simeq 0.7$ or $k_\theta \rho_s = 1.36$ which is at the limit of the short ion scales. Nonetheless, as we will see, the fine structures near MRSs which are present on the different toroidal Fourier components $\delta\hat{\phi}(s, \theta^\star, n)$ are arbitrarily small with respect to the maximum simulated mode number n, because the distance between MRSs is proportional to $r/\hat{s}q_s n$. This physics of the passing electrons near MRSs hinder small scales polarization effects which require the use of the arbitrary wavelength solver. These fine structures present on $\delta\phi$ can have a radial width smaller than an ion Larmor radius, which corresponds to $k_r \rho_i \gtrsim 6$. The main rationale for only simulating the toroidal mode numbers $n \lesssim 44$ in a half torus tokamak, is to reduce the cost of the simulation carried out with the Deuterium to electron mass ratio.

2. *Quasi-linear flux estimate*

The radial turbulent transport of particles can be seen as the result of a phase shift between the perturbed species density and the perturbed electrostatic potential. A way of predicting the presence of radial transport due to an electrostatic perturbation can be based on the measurement of the phase shift between the perturbed density and the perturbed electrostatic potential, *i.e.*, $arg(\delta\hat{N}/\delta\hat{\phi})$, where the Fourier representation of the field, *i.e.*, $\delta\hat{N}$ and $\delta\hat{\phi}$, has been employed. Note that when $\pi > arg(\delta\hat{N}/\delta\hat{\phi}) > 0$ the radial flux is outward and when $0 > arg(\delta\hat{N}/\delta\hat{\phi}) > -\pi$ the radial flux is inward, according to the definition of the quasi-linear perturbation transport

$$\hat{\Gamma}^{\mathrm{ql}} \simeq \frac{-\imath\,k_y}{B}\delta\hat{\phi}^*\delta\hat{N} = \frac{-\imath\,k_y|\delta\phi|^2}{B}\frac{\delta\hat{N}}{\delta\hat{\phi}}, \tag{32}$$

with k_y the wavenumber in the binormal direction $\mathbf{y} = \mathbf{b} \times \nabla s/|\nabla s|$.

For studying the turbulent electron fluxes organization, it turns out to be relevant to split the electron density perturbation into the four following subgroups: passing electrons with $E_{\mathrm{kin}} = m_e v_{\parallel}^2/2 + \mu B_0 \leq T_e(\mathbf{X})$, passing electrons with $E_{\mathrm{kin}} > T_e(\mathbf{X})$, trapped electrons with $E_{\mathrm{kin}} \leq T_e(\mathbf{X})$, and trapped electrons with $E_{\mathrm{kin}} > T_e(\mathbf{X})$. The density perturbation of these groups are plotted in Fig. 18.

We are now interested to identify the phase shift between $\delta\phi$ and δN_e in global linear ORB5 simulations. In Fig. 18, the kinetic response of passing electrons shown in subplot (a) for $E_{\mathrm{kin}} \leq T$ and (b) for $E_{\mathrm{kin}} > T$ are both composed of adiabatic and nonadiabatic components. The adiabatic component corresponds to the large structures comparable to the ones observed on $\delta\phi$ in subplot (f). The nonadiabatic passing-electron component is radially localized on the different lowest order MRSs of this $n = 16$ eigenmode. The MRSs can be easily localized by identifying the layer of parallel current $\delta u_{\parallel}$ in subplot (e). It is also noticeable that this shift is counter-clockwise for $E_{\mathrm{kin}} \leq T_e(\mathbf{X})$ and clockwise for $E_{\mathrm{kin}} > T_e(\mathbf{X})$. In comparison, the trapped electron population is also split into the same subthermal and suprathermal subgroups, respectively $E_{\mathrm{kin}} \leq T_e(\mathbf{X})$ and $E_{\mathrm{kin}} > T_e(\mathbf{X})$. It clearly appears in subplots (c) and (d) that the phases of these trapped electron subgroups kinetic responses are of opposite signs. Moreover, the trapped electron subthermal group density perturbation is localized at a more inward radial position than the density perturbation of the suprathermal group kinetic response. The phase shift of these thermal subgroups
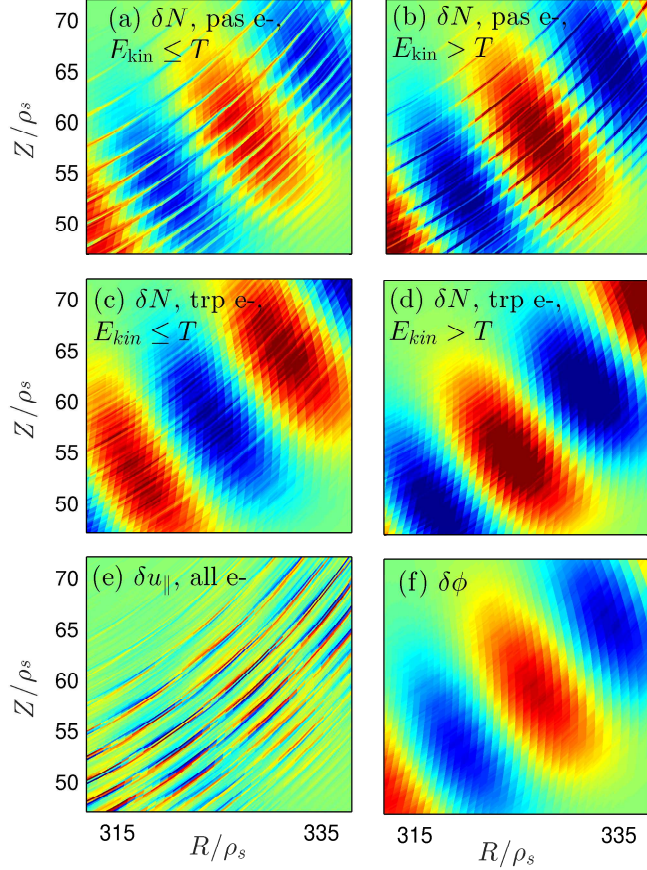
31

FIG. 18. Electron density perturbation split into four subgroups: (a) passing electrons with $E_{\text{kin}} \leq T_e$, (b) passing electrons with $E_{\text{kin}} > T_e$, (c) trapped electrons with $E_{\text{kin}} \leq T_e$, (d) trapped electrons with $E_{\text{kin}} > T_e$. Subplot (e) electron parallel current $\delta u_\parallel$. Subplot (f) $\delta \phi$. Linear TCV simulation physical mass ratio $m_i/m_e = 3672$, and $n = 16$. Note that the electron subgroup densities (a-d) are obtained from new diagnostics in which the fluid moments are computed on the same DFT finite-elements representation than the one which is used to represent the electrostatic field $\delta \phi$ and to copute the right-hand-side of the QNE. It gives an insight on the "smoothness" of each subgroup contributions to the charge assignment when computing the self consistent electrostatic field $\delta \phi$ (f).

being of opposite signs these thermal subgroup contributions to the particle transport will be in opposite directions, as we will confirm in nonlinear simulations.

It is of interest to look at the cause for having different phase-shift signs, $sign(arg(\delta N_e/\delta \phi))$, between the subthermal and suprathermal subgroups of particles. For simplicity, we carry out this analysis at the MRS $q_s = 3/2$ which is of lowest order in a half torus simulation so
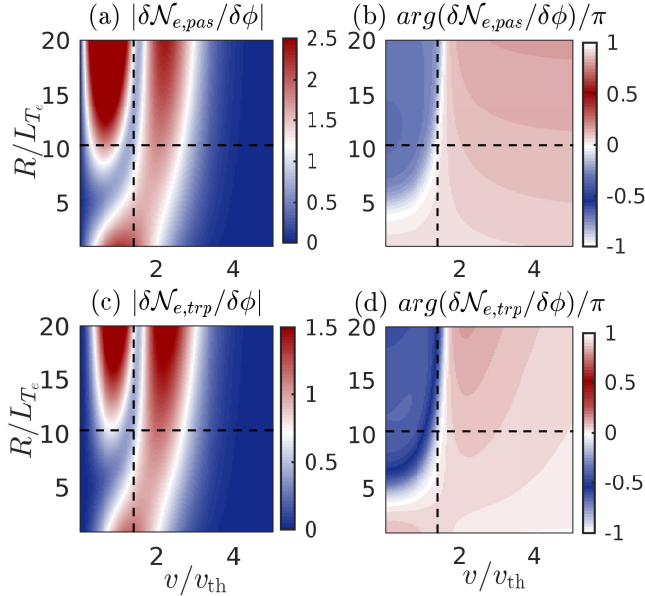
32

FIG. 19. Amplitude (a,c) and phase (b,d) of the nonadiabatic electron response of passing electrons $\delta N_{e,pas}/\delta\phi$ (a,b) and trapped electrons $\delta N_{e,trp}/\delta\phi$ (c,d). Results obtained with a local dispersion relation analysis at the radial position $q_s = 1.5$ where $k_\parallel R q_s = 0$. The horizontal line indicates the value of the TCV electron temperature gradient taken at $q_s = 3/2$ from CHEASE input file. The vertical line indicates the position at which $v = \sqrt{2T/m}$ which is the boundary we have chosen for further dissociating the subthermal and suprathermal subgroups of electrons.

that $k_\parallel = 0$. This analysis of the phase shift between $\delta\phi$ and δN_e is carried out with the local dispersion relation

$$
0 = \frac{ZT_{i0}}{T_{e0}} + 1 - \frac{T_{i0}}{T_{e0}} \int d^3v \, J_0^2(k_\perp\rho_i) \frac{\omega - \omega_i^\star}{\omega - k_\parallel v_\parallel - \omega_{di}} \frac{f_{i0}}{N_{i0}}
$$
$$
+ \left(1 - \frac{\omega_e^\star}{\omega}\right) \left[\alpha_t z_{be}^2 W(z_{be})\right]
$$
$$
+ \left(1 - \frac{\omega_e^\star}{\omega}\right) \left[-1 + \alpha_t + W(z_e) - \alpha_t W\left(\frac{z_e}{\alpha_t}\right)\right], \tag{33}
$$

which includes fully kinetic species responses and is described in detail in Ref. 5. In this equation α_t is the fraction of trapped electrons, $\omega_{di} = -k_\perp(v_\parallel^2 + v_\perp^2/2)/\Omega_0 B_0 R$, $z_{be} = \text{sgn}(\omega_{\varphi e})\sqrt{2\omega/\omega_{\varphi e}}$, $\omega_{\varphi e} \simeq \omega_{Ne} L_N/R$, $z_e = \omega/k_\parallel v_{the}$, and $W(z)$ is the dispersion function. The *nonadiabatic response of the passing electrons, i.e.* the third line of Eq. (33), was obtained from the nonadiabatic electron response

$$
\delta g_e(\vec{v}, R/L_{T_e}) = -N_{e0} \frac{e\delta\phi}{T_{e0}} \frac{\omega - \omega_e^\star}{\omega - k_\parallel v_\parallel} \frac{f_{e0}}{N_{e0}}, \tag{34}
$$

where the electron temperature gradient dependency is contained in the diamagnetic drift

$$\omega_e^\star = \omega_{Ne}[1 + \eta_e(\tilde{E} - 3/2)],$$

$\omega_{Ne} = T_{e0}k_\perp/eB_0L_N$, $\eta_e = L_{N_e}/L_{T_e}$, $\tilde{E} = mv^2/2T$, and $v = \sqrt{v_\perp^2 + v_\parallel^2}$. At MRSs, where $k_\parallel = 0$, we observe that this local nonadiabatic response does not depend on the pitch angle λ so that one defines the quantity

$$\frac{\delta\mathcal{N}_{e,pas}(v, R/L_{T_e})}{\delta\phi} = -(1 - \alpha_t)\frac{e}{T_{e0}}4\pi v^2\frac{\omega - \omega_e^\star}{\omega}f_{e0}(v). \tag{35}$$

The *nonadiabatic response of the trapped electrons, i.e.* the second line of Eq. (33), was obtained from the nonadiabatic bounce-averaged trapped electron response which is here taken in its form independent of the pitch angle

$$\frac{\delta\mathcal{N}_{e,trp}(v, R/L_{T_e})}{\delta\phi} = -\alpha_t\frac{e}{T_{e0}}4\pi v^2\frac{\omega - \omega_e^\star}{\omega - n\langle\dot{\varphi}\rangle}f_{e0}(v), \tag{36}$$

see Ref. 5 and references therein for details. From these velocity-dependent contributions to the electron density perturbation, one can recover the local electron density perturbation with the equation $\delta N_e = (eN_{e0}\delta\phi/T_{e0}) + \int dv\delta\mathcal{N}_{e,trp} + \int dv\delta\mathcal{N}_{e,pas}$. In the spirit of the quasi-linear estimate of the turbulent particle flux, a value of the velocity for which the imaginary part of $\delta\mathcal{N}_e/\delta\phi$ is nonzero will contribute to the radial transport. In Fig. 19, the velocity-dependent responses $\delta\mathcal{N}_{e,trp}$ or $\delta\mathcal{N}_{e,pas}$ are scanned with respect to the gradient R/L_{T_e}. Represented are the absolute value $|\delta\mathcal{N}_e/\delta\phi|$ and the phase shift $arg(\delta\mathcal{N}_e/\delta\phi|)/\pi$. These subplots clearly show that a transition occurs around $R/L_{T_e} \simeq 6$. For $R/L_{T_e} > 6$, there are two local maxima of $|\delta\mathcal{N}_e/\delta\phi|$, and these two subgroups have phase shifts $arg(\delta\mathcal{N}_e/\delta\phi)/\pi$ of opposite signs. From this observation these two subgroups might contribute to the flux in opposite directions thus potentially canceling each other. For small values of the gradient, $R/L_{T_e} \leq 6$, the nonadiabatic electron response is essentially homogeneous in the v direction: there is only one maximum on $|\delta\mathcal{N}_e/\delta\phi|$ and the phase shift $arg(\delta\mathcal{N}_e/\delta\phi)/\pi$ is nearly constant. The rationale to the presence of two energetic subgroups which contribute to the quasi-linear flux in opposite directions for big values of R/L_{T_e} is due to the physics described by the diamagnetic drift which is velocity- and gradient-dependent. In our TCV test case, $\eta_e \simeq 2$ so that $\omega_e^* \simeq 2\omega_{Ne}(\tilde{E} - 1)$ which shows that it is of opposite sign for suprathermal and subthermal electrons.
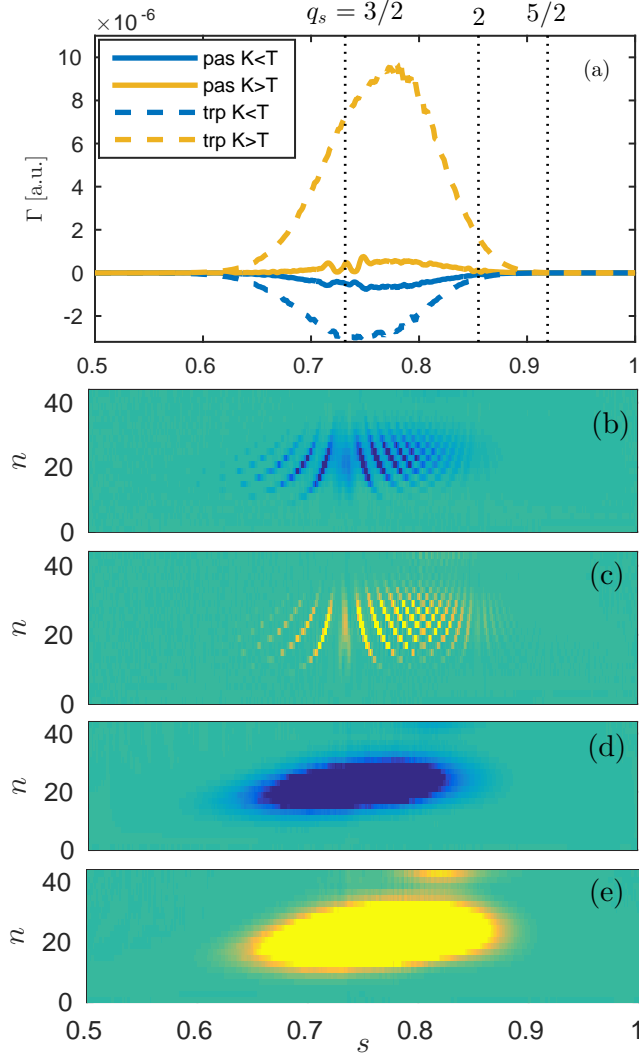
FIG. 20. Turbulent particle transport during the linear regime, $tc_s/a \simeq 17$, of the nonlinear simulation of TCV carried out with the D/e^- mass ratio. Subplot (a) is the time averaged turbulent particle flux contributions from the different subgroup of electrons: passing with $E_{\mathrm{kin}} \leq T_e$, passing with $E_{\mathrm{kin}} > T_e$, trapped with $E_{\mathrm{kin}} \leq T_e$, and trapped with $E_{\mathrm{kin}} > T_e$. The time averaged spectra is plotted at each radial position for these same subgroups in subplot (b), (c), (d), and (e), respectively. Color code: blue for inward flux, yellow for outward flux, and green for zero flux. The amplitude (colorbar) has been chosen such as to reveal the radial structures.

3. Turbulent particle electron flux in the linear growing phase of the nonlinear simulation

For electrons, the turbulent particle flux, Eq. (26) with $\mathcal{A} = 1$, can be approximated using $B_\parallel^\star \simeq B$ and $\langle \phi \rangle \simeq \phi$, thus $\dot{\mathbf{X}} \simeq -\nabla\phi \times \mathbf{b}/B$, and $\Gamma_e \simeq \langle \delta N_e \dot{\mathbf{X}} \cdot \nabla s/|\nabla s| \rangle_{\mathcal{S}}$. The electron turbulent fluxes are then decomposed into their subthermal and suprathermal subgroup contributions, by using the new 3D diagnostics which are based on the finite elements representation of the fields δN and $\delta\phi$.

Thanks to these new turbulent flux diagnostics, the predictions made in the previous quasi-linear analysis, that subthermal and suprathermal subgroups of electrons contribute to the particle flux in opposite directions, are confirmed in global ORB5 nonlinear simulations when looking at the instantaneous turbulent flux, taken at $tc_s/a \simeq 17$, *i.e.* during the regime of linear growth, see Fig. 20 (a). The subthermal particles have an inward flux and the suprathermal ones have an outward flux. For passing electrons, these thermal subgroups contributions to the flux cancel each other and the total passing electron particle flux is essentially negligible. For trapped electrons, the subthermal electron also have an inward flux, but globally the electron particle flux is dominated by the suprathermal trapped electron contribution, which is outward.

These subgroup contributions to the particle flux are also split in their toroidal-spectral components, in subplots (b-e). Each subplot is a mixed representation: direct in the radial direction and discrete Fourier in the toroidal direction. This spectral-radial representation is computed from equation

$$\tilde{\Gamma}_e(s, n) \approx \oint d\theta^\star \bar{\mathcal{J}} \delta \hat{N}^*(s, \theta^\star, n) \frac{-\nabla \delta \hat{\phi}(s, \theta^\star, n) \times \mathbf{B}}{B^2} \cdot \nabla s,$$

where Parseval theorem has been employed to replace the integral over the toroidal direction, $\Gamma_e(s) = \sum_n \tilde{\Gamma}_e(s, n)$, $\bar{\mathcal{J}} = \mathcal{J}/\langle |\nabla s| \rangle_{FS}$, and one made the approximation $B_\parallel^\star \simeq B$ in the denominator of the electric drift.

It is remarkable that the passing electron contribution to the particle turbulent flux is solely localized near the MRSs of each toroidal mode number n. As a result, for bigger n there are more surfaces for which the passing electrons contribute to the turbulent transport. This turbulent flux of passing electrons is thus organized in a structured manner as illustrated by this $\tilde{\Gamma}_e(s, n)$. Note that the radial width of the fine structures near MRSs are thinner

in the case of suprathermal particles because these fast particles are more akin to respond adiabatically.

An important remark is that the passing electron turbulent flux is sustained by radially localized contributions coming from the different mode numbers n, but that the sum of these "discrete" contributions has a remarkably smooth radial profile, see subplot (a). This smoothness of the overall passing electron profile of turbulent flux emphasizes the existence of a strong interplay between the different toroidal modes composing the spectra. The trapped electron contribution to the turbulent flux is not showing such a clear organization near the lowest order MRSs.

4. Turbulent particle electron flux in the turbulent saturated regime of the nonlinear simulation

The turbulent particle flux in the turbulent saturated regime is following the same organization as in the linear regime. The subthermal electrons carry an inward flux and the suprathermal electrons carry an outward flux. The subthermal and suprathermal passing electron contributions to the particle flux cancel each other, and the trapped suprathermal electron contribution dominates the particle transport with a resulting outward flux. The radial spectra show that the passing electron channel of transport has the same particular organization: both thermal subgroups of passing electrons have a radially smooth profile of turbulent transport $\Gamma_e(s)$, but at each radial position s only the resonant toroidal mode numbers n contribute to this transport. For example, in this half torus simulation all the toroidal modes n can carry a turbulent flux at the lowest order MRSs $q_s = 3/2$, 2, 5/2, 3, and 7/2, but at the second order MRSs, for example $q_s = 3/4$, only half of the spectra can carry a turbulent transport.

In Fig. 22, the turbulent particle transport obtained from nonlinear simulations carried out with the physical mass ratio are compared to the one obtained in simulations carried out with the heavy electrons mass ratio. Basically, when increasing the electron mass, the transport significantly increases in all the channels of transport, up to a factor 2-3 for the passing electrons. On the other hand, the overall particle flux is increased by only $\simeq 15\%$, but the overall gradients are relaxing much faster, see Fig. 15. This increase of the turbulent flux in spite of lower gradient is clearly a sign that the turbulent diffusivity is higher in the
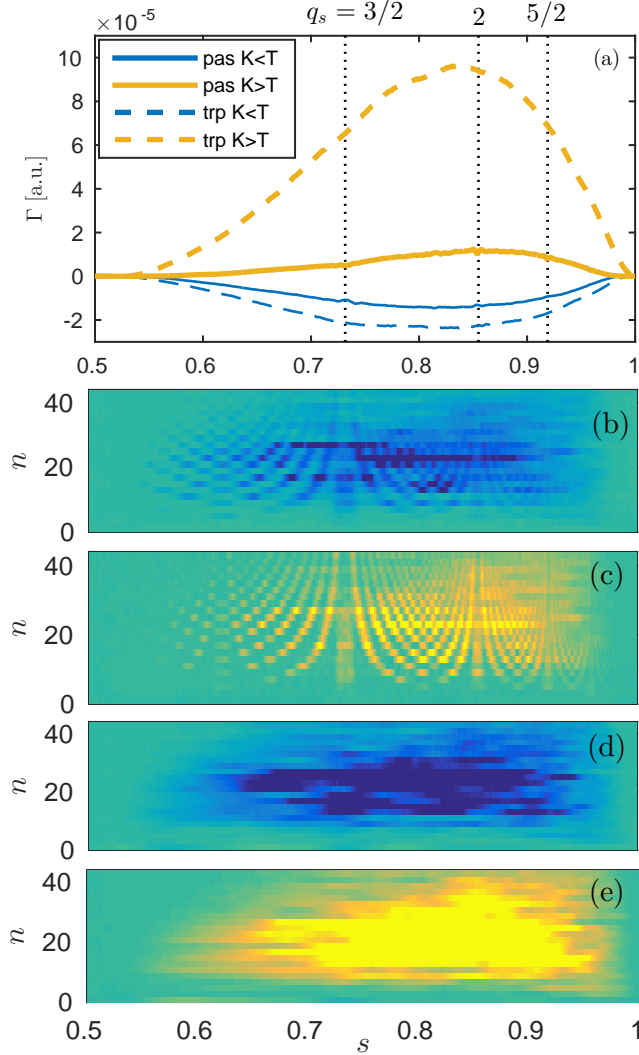
FIG. 21. Turbulent particle transport time-averaged over the turbulent saturated regime, $tc_s/a > 70$ from the same simulation than in Fig. 20. Same subplots than in Fig. 20.

case of the heavy electron mass ratio $m_i/m_e = 400$, in particular for the passing electron channel.

We observe that the total passing electron contribution to the turbulent particle flux is essentially negligible for both mass ratios. Nonetheless, because the suprathermal passing electrons systematically go outside and the subthermal systematically go inside, the passing electrons contribute by $\simeq 11\%$ and 27% to the total electron turbulence heat flux, with $m_i/m_e = 3672$ and 400, respectively. In absolute value the passing electron heat flux is $\simeq 3$ times bigger with the heavy electrons than with real electrons, and the trapped electron contribution is only $\simeq 10\%$ bigger. The passing electrons thus contribute significantly to
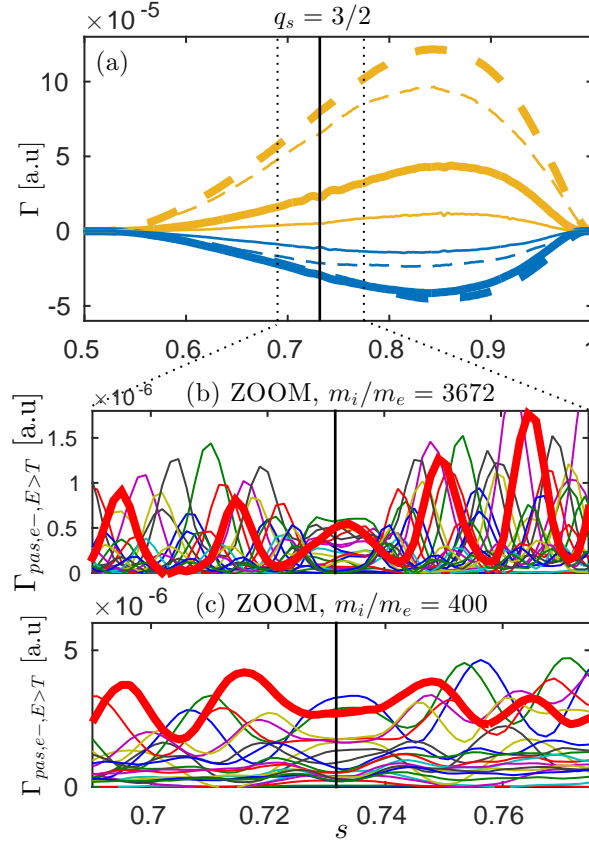
38

FIG. 22. Comparison of the turbulent electron particle flux between nonlinear simulations carried out with heavy electrons $m_i/m_e = 400$ (thick line in subplot (a)) and the Deuterium/electron mass ratio $m_i/m_e = 3672$ (thin line in subplot (ab)). Same color code in subplot (a) than in subplot (a) of Fig. 20. The radial profile of each toroidal mode number n contribution to the suprathermal passing electron, *i.e.* $\tilde{\Gamma}_{pas,e-,E>T}(s,n)$ is plotted in subplot (b) for the D/e- physical mass ratio and in subplot (c) for the heavy electron mass ratio. In subplot (b) and (c) the contribution from the toroidal mode number $n = 12$ is represented with a red thick line.

the overestimate of the turbulence heat flux measured in simulation carried out with heavy electrons.

In the case of the *passing electron* channel of turbulent transport, heavy electrons being $\simeq 9$ times heavier than real ones their thermal speed is $\simeq 3$ times slower and the radial width of the fine structures of nonadiabatic passing electron response are $\simeq 3$ times larger. As a consequence one can roughly estimate that a given toroidal mode number n will be "turbulence conducting" over a radial region roughly $\simeq 3$ times larger when using the heavy electrons. This local influence of the mass ratio over the radial profile of passing electron

turbulence transport is illustrated in Fig. 22 subplot (b) and (c), where the radial profile of turbulent particle flux is plotted for each mode n composing the simulation spectra. It appears, in particular for the mode number $n = 12$ highlighted with red thick lines, that the turbulent flux contribution of each mode number n composing the turbulence spectra are localized near the lowest order MRSs proper to each mode number. A significant difference when using the heavy electrons is that the radial width of these "fine" structures of nonadiabatic passing electron response are larger than the distance between their respective lowest order MRSs. In comparison, for the real electron mass, the fine structures present on the simulated modes ($n \leq 44$) are always thinner than the distance between consecutive MRSs (except for biggest values of n in the region of high shear). When summing these mode number contributions to the passing-electron turbulent flux, the resulting particle flux is radially smooth (a) despite the fact that the density of modes to which the passing electrons respond nonadiabatically is varying radially. Finally, one can assume that the turbulence diffusivity D_{turb} of the whole plasma is proportional to the density of resonant mode number n which can carry turbulence. As a consequence this turbulence diffusivity should be radially more corrugated in case of D/e- mass ratio because in this case the nonadiabatic structures are thinner and thus radially more sparse. If the flux, Γ, is radially smooth but the turbulence diffusivity, D_{turb}, is radially corrugated, then the radial profile of gradient, $d \ln N/ds$, should compensate these corrugations so that $\Gamma = D_{\mathrm{turb}}(-d \ln N/ds)$ is smooth. A direct observation of such a property of the gradients can be made when looking at the density and temperature gradients in Fig. 23 subplots (c) and (d).

In the case of the *trapped electron* channel of turbulent transport, the main resonance causing the trapped electron destabilization is located near $E_{\mathrm{kin}} \simeq 2.5 T_e$. In their rapid motion along the field line, the trapped electrons are essentially similar to the passing electrons thus explaining the fact that the subthermal and suprathermal subgroups follow the quasi-linear prediction of carrying out an inward flux and an outward flux, respectively. In their slow bounce-averaged motion these trapped electrons have nonetheless a different nonadiabatic response to the field perturbation, explaining why they do not have the same radial spectra as the ones of the passing electrons, *i.e.* turbulent flux contributions localized near lowest order MRSs.
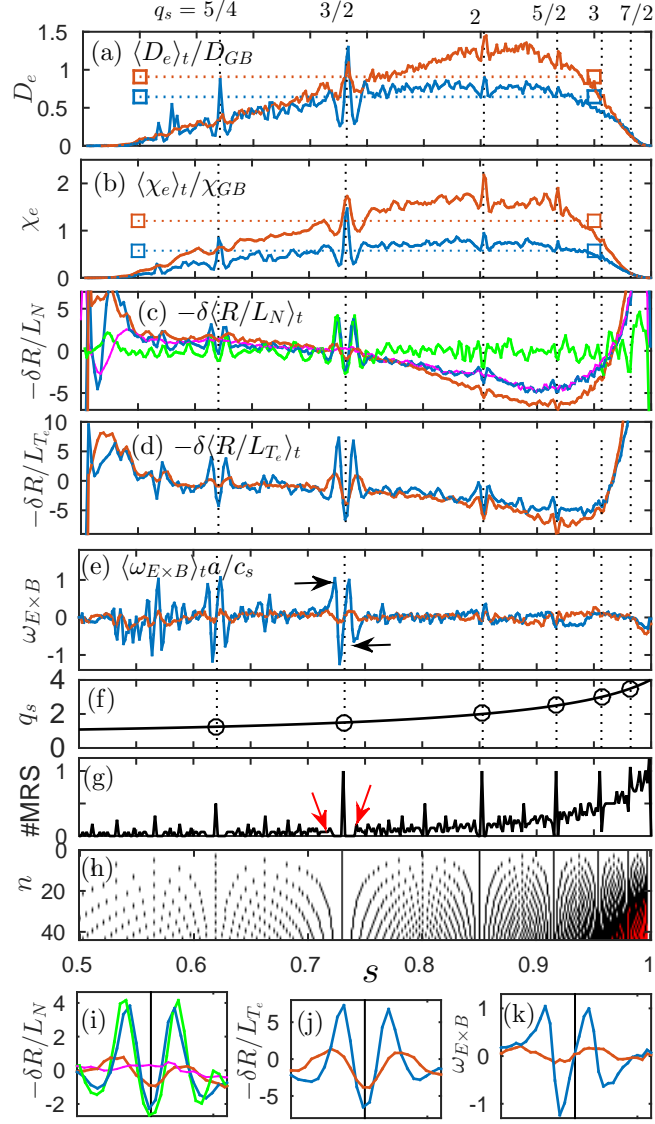
FIG. 23. [Color online] Nonlinear simulation of half-torus with physical D/e⁻ mass ratio (blue) and heavy electrons (red). Subplots time-averaged of the (a) electron particle diffusivity, (b) electron heat diffusivity, (c) perturbed particle density gradient (green contribution of the ion polarization and magenta contribution from the ion gyrodensity for simulation with $m_i/m_e = 3672$), (d) perturbed electron temperature gradient, (e) $E \times B$ ZF shearing rate. Subplot (f) the safety factor. Subplot (g) the number of MRSs per radial interval $[s, s+\Delta s]$ divided by the number of simulated toroidal mode numbers. A surface is rational for a mode number n if there exist a poloidal mode number m such that $q_s = m/n$. Only the simulated mode numbers are considered. In subplot (h), plotted is the contribution from each simulated mode number n decomposition to the subplot (g), color code: white 0, black for 1, and red for 2 and more. Half torus simulations. Subplots (i), (j), and (k) are Zoom on the $q_s = 3/2$ surface of the subplots (c), (d), and (e), respectively.

41

5. Zonal flows organization

In Fig. 23, plotted are the time-averaged radial profiles of the electron particle diffusivity (a), the electron heat diffusivity (b), the density gradient perturbation (c), the electron temperature gradient perturbation (d), the $E \times B$ ZF shearing rate (e), the safety factor (f), the MRSs density (g), and the MRSs density per mode number (h). Two simulations with physical electron mass (blue curves) and heavy electron mass (red curves) are presented.

It is remarkable in subplots (c,d,e) of this figure, that the time-averaged radial profiles of the electron temperature gradient perturbation, $\langle \delta R/L_{T_e} \rangle_t$, density gradient perturbation, $\langle \delta R/L_N \rangle_t$, and $E \times B$ zonal flow (ZF) shearing rate, $\langle \omega_{E \times B} \rangle_t$, show the same organization near lowest order MRSs, $q_s = 5/4, 3/2$, and 2, than already shown in flux-tube geometry[5,34]: a steepening-flattening-steepening of the gradients and the $E \times B$ shearing rate which is zero at MRS and maximum just before and after. See the zooms in subplots (i), (j), and (k). The presence of these fine structures near low order MRSs on the radial profile of ion polarization density $\delta R/L_{N,pol}$ and on $E \times B$ ZF shearing rate explains the importance of using the new arbitrary wavelength solver. For example, the distance between the local maxima of the gradient of ion polarization density, $\delta R/L_{N,pol}$ (green curve), located just before and after the $q_s = 3/2$ surface is of about $\simeq 2\rho_i$.

When analyzing the passing electron turbulent particle flux, in the previous section, we did not use the ZF saturation mechanism argument for explaining the reduction of turbulent transport. We rather showed that this reduction of passing electron turbulent transport is related to a rarefaction of the radial region of nonadiabatic passing electron response, *i.e.*, the regions where the different spectral modes can sustain a turbulent transport. In turns this sparsity of the fine radial structures of passing electron turbulent transport is associated to the presence of fine zonal flow structures near low order MRSs, which furthermore quench the turbulence. In other words, the reduction of passing electron turbulence diffusivity causes a local steepening of the plasma kinetic profiles on either side of the low order MRSs, which then reinforces the ZF shearing rate there and thus furthermore reduces the transport. This can be seen as a nonlinear feedback reducing the turbulence transport. In an opposite manner, at the low order MRSs, heat diffusivity is enhanced, which causes a flattening of the profiles, noting that the ZF shearing rate is vanishing there, see Fig. 23(k).

Despite the fact that these fine ZFs structures have a different amplitude when modifying

the electron mass, their radial width remains essentially the same, see the black arrows in Fig. 23 subplot (e). Moreover, in the region of low shear, these ZFs radial widths are typically larger in nonlinear simulations than in linear simulations, as already observed in Ref. 5. It is rather interesting to point out that these structure widths seem to be related to the topology of the magnetic field and in particular to the local density of MRSs. It appears that these ZFs structures fit in a radial gap surrounding the low order MRS where no other MRS is simulated. The gap associated to the MRS $q_s = 3/2$ is identified with red arrows in subplot (g). A similar observation can be made for surfaces $q_s = 5/4, 2, 5/2$, in simulations carried out with either the physical mass ratio or heavy electrons. This gap between MRSs is also clearly illustrated in subplot (h) for each toroidal mode number n. When such a gap exists in the magnetic topology, the destabilizing influence of the low order MRS on the passing electron dynamics seems more significant.

The ZFs structures are known to saturate the turbulence by $E \times B$ ZFs shearing. It is therefore worth pointing out that with the light electrons, the level of transport is significantly lower and the $\omega_{E \times B}$ is significantly higher than with the heavy electrons. Comparing the simulation results obtained with the two different mass ratios, it appears that these ZFs and gradient structures located near low order MRSs have a $\simeq 3$ times bigger amplitude in simulation carried out with the real electron mass, see Fig. 23 (c,d,e) in particular near $q_s = 3/2$ and $5/4$.

V. CONCLUSION

A *new arbitrary wavelength field solver* has been implemented in the ORB5 code which allows the study of quasi-neutral micro-turbulence at arbitrarily short scales in $k_\perp \rho_i$. The linearized polarization drift contribution to the quasi-neutrality equation is now accounted for in its integral form. The new solver implementation has been described in detail and the particular requirements to converge the electrostatic field solution on axis and near the edge have been discussed. The behavior of the solution at the boundary has also been discussed for the integral operator. The option of using the Padé approximation for computing the ion polarization drift contribution to the quasi-neutrality equation is also available when running simulations with the fully kinetic electron model.

A *benchmark of the gyrokinetic code ORB5* with this new solver has been carried out

against the global version of the gyrokinetic code GENE, in realistic ideal MHD toroidal geometry. This benchmark was conducted in the ITG to TEM part of the instability spectra ($0 < k_\theta \rho_s < 1.5$). The three different electron models, *i.e.* adiabatic, hybrid, and kinetic, have been used to study the short scale physics of the nonadiabatic responses of either the trapped electrons or the passing electrons. In each case a very good quantitative agreement has been found between GENE and ORB5 when using the new arbitrary wavelength solver. A good quantitative agreement has also been found with the Padé version of the solver which is implemented for the kinetic electron model only. As expected, the long wavelength version of the solver totally fails at resolving the short scale physics due to the nonadiabatic response of both trapped electrons and passing electrons. In this benchmark, it was also shown that the TEM branch is more unstable when using the fully-kinetic electron model than when using the hybrid model. This increase of the destabilization is due to the fact that a large fraction of the passing electron population has a nonadiabatic response to the perturbation. This reduction of the global adiabatic response of the passing electrons has a destabilizing effect as discussed in flux tube geometry[5].

Nonlinear electrostatic simulations for conditions relevant to TCV have been carried out with the heavy electrons, $m_i/m_e = 400$, the new solver, and the kinetic model for both the ions and the electrons. It was shown that using the Padé solver is essentially equivalent than using the arbitrary wavelength solver for the considered test case, and that to correctly simulate the physics of passing electrons near mode rational surfaces, one must account for the whole mode numbers composing the toroidal spectra. The rationale being that the density of mode rational surfaces is different in a full torus than in a half torus. As a non realistic consequence, in a half torus simulation, the nonadiabatic passing electron response is not properly modeled, in particular for comparison with experiments.

Physical deuterium to electron mass ratio ($m_i/m_e = 3672$) simulations of this TCV relevant test case have been carried out with the fully kinetic model and the arbitrary wavelength solver. The particular radial organization of the passing electron turbulent flux spectrum and its strong ties with the radial profile of safety factor are revealed. Each toroidal mode number n contributes to the passing electron turbulent flux only near its associated lowest order MRSs, *i.e.* where the passing electron respond nonadiabatically. The whole turbulent flux spectrum is organized such as to ensure a radially smooth profile of passing electron turbulent flux, despite the radial sparsity of each mode contribution to the flux. At lowest

order MRSs the turbulence diffusivity, D_{turb}, is maximum because all the modes composing the spectrum can be nonadiabatic and thus "conduct" turbulence, whereas at highest order MRSs (for example just before and after the lowest order MRSs) the turbulence diffusivity is minimum because only a few toroidal mode numbers can be nonadiabatic and thus "conduct" turbulence. To ensure a smooth radial profile of turbulent transport, the gradients which drive this turbulent flux are corrugated so that $\Gamma = -(\delta R/L_N) D_{\text{turb}}$ is smooth. The organization is actually a bit more complex because the turbulence diffusivity will be locally increased or decreased, by the local steepening or flattening of the gradient, respectively. These strong radial corrugations of the gradients near MRSs are associated to the formation of internal transport barriers of strong amplitude. These fine zonal flows structures due to the nonadiabatic passing electron response near MRSs are strongly amplified in nonlinear simulation carried out with the realistic mass ratio compared to simulations carried out with heavy electrons. The time- and radial-averaged $E \times B$ zonal flow amplitude $\langle\langle|\omega_{E\times B}|\rangle_s\rangle_t$ is increased by $\simeq 25\%$, the radial averaged amplitude of the long-time-averaged $E \times B$ zonal flow $\langle|\langle\omega_{E\times B}\rangle_t|\rangle_s$ is increased by a factor $\gtrsim 2$. A decrease of the level of turbulence is associated to this increase of ZFs saturating dynamics: the level of electron turbulent heat flux is decreased by a factor $\simeq 2$. The time-averaged turbulent particle flux $\langle\Gamma\rangle_t$ is not significantly increased ($\simeq 10\%$) but its associated turbulent diffusivity is, by $\simeq 30 - 40\%$, as a consequence of profile relaxation. It is thus necessary to use the physical mass ratio for correctly simulating the turbulence and its associated transport level.

The *influence of the electron diamagnetic drift* over the internal electron turbulent transport organization is shown, by means of quasi-linear flux estimate which predictions are confirmed in nonlinear global ORB5 simulations. At high values of the electron temperature gradient, for example $R/L_{T_e} \simeq 11$ when studying the magnetic surface $q_s = 3/2$, the electron velocity phase space is organized in two subgroups: the subthermal and the suprathermal electrons. The particularity of this organization is that the two subgroups contribute to the quasi-linear flux in opposite directions, potentially canceling each other. Moreover, when reducing the electron temperature gradient, the velocity phase space organization transits toward a single subgroup organization which carry a quasi-linear flux in one direction essentially. This feature is common to the trapped and passing electrons, thus emphasizing the role of the diamagnetic drift on the flux direction. In *nonlinear global simulations* carried out with ORB5, the passing electron turbulent flux was found to be essentially zero.

Nonetheless, the particle flux contributions from the subthermal and suprathermal passing electrons represent each a significant fraction of the total turbulent transport. This observation is of prime importance because these fluxes, of opposite directions, will trigger radial corrugation near low order MRSs in order to ensure a smooth radial profile of particle flux. If the particle fluxes of both these subgroups was zero, no radial corrugations on the profiles would have been necessary for ensuring a smooth radial flux, thus potentially canceling the existence of the ZFs structures and associated internal transport barriers. Finally it was shown that this particular organization of the passing electron channels does not contribute to the particle flux, but rather contributes to the turbulence heat flux, up to 30%.

VI.   ACKNOWLEDGMENT

REFERENCES

[1]T. Görler, Ph.D. thesis, University of Ulm, Germany (2009).

[2]N. T. Howard, C. Holland, A. E. White, M. Greenwald, and J. Candy, Physics of Plasmas **21**, 112510 (2014).

[3]S. Maeyama, Y. Idomura, T.-H. Watanabe, M. Nakata, M. Yagi, N. Miyato, A. Ishizawa, and M. Nunami, Phys. Rev. Lett. **114**, 255002 (2015).

[4]N. Howard, C. Holland, A. White, M. Greenwald, and J. Candy, Nuclear Fusion **56**, 014004 (2016).

[5]J. Dominski, S. Brunner, T. Görler, F. Jenko, D. Told, and L. Villard, Physics of Plasmas **22**, 062303 (2015).

[6]T. Tran, K. Appert, M. Fivaz, G. Jost, J. Vaclavik, and L. Villard, Theory of Fusion Plasmas, Int. Workshop (Bologna Editrice Compositori,Società Italiana di Fisica) p. 45 (1999).

[7]S. Jolliet, A. Bottino, P. Angelino, R. Hatzky, T. Tran, B. Mcmillan, O. Sauter, K. Appert, Y. Idomura, and L. Villard, Computer Physics Communications **177**, 409 (2007).

[8]A. Bottino, B. Scott, S. Brunner, B. McMillan, T. Tran, T. Vernay, L. Villard, S. Jolliet, R. Hatzky, and A. Peeters, Plasma Science, IEEE Transactions on **38**, 2129 (2010).

[9]B. F. McMillan, S. Jolliet, T. M. Tran, L. Villard, A. Bottino, and P. Angelino, Physics of Plasmas **15**, 052308 (2008).

[10]B. McMillan, S. Jolliet, A. Bottino, P. Angelino, T. Tran, and L. Villard, Computer Physics Communications **181**, 715 (2010).

[11]T. Vernay, S. Brunner, L. Villard, B. F. McMillan, S. Jolliet, T. M. Tran, A. Bottino, and J. P. Graves, Physics of Plasmas **17** (2010).

[12]J. Collier, Ph.D. thesis, University of Warwick, United Kingdoms (2015).

[13]M. Fivaz, S. Brunner, G. de Ridder, O. Sauter, T. Tran, J. Vaclavik, L. Villard, and K. Appert, Computer Physics Communications **111**, 27 (1998), ISSN 0010-4655.

[14]A. Mishchenko, A. Könies, and R. Hatzky, Physics of Plasmas **12**, 062305 (2005).

[15]Z. Lin and W. W. Lee, Phys. Rev. E **52**, 5646 (1995).

[16]F. Jenko, W. Dorland, M. Kotschenreuther, and B. N. Rogers, Physics of Plasmas **7**, 1904 (2000).

[17]T. Görler, X. Lapillonne, S. Brunner, T. Dannert, F. Jenko, F. Merz, and D. Told, Journal of Computational Physics **230**, 7053 (2011).

[18]F. Hofmann, J. B. Lister, W. Anton, S. Barry, R. Behn, S. Bernel, G. Besson, F. Buhlmann, R. Chavan, M. Corboz, et al., Plasma Physics and Controlled Fusion **36**, B277 (1994).

[19]T. S. Hahm, M. A. Beer, Z. Lin, G. W. Hammett, W. W. Lee, and W. M. Tang, Physics of Plasmas **6**, 922 (1999).

[20]A. J. Brizard and T. S. Hahm, Rev. Mod. Phys. **79**, 421 (2007).

[21]M. Lebrun and T. Tajima, Bull. Am. Phys. Soc. **39**, 1533 (1995).

[22]W. Horton, Rev. Mod. Phys. **71**, 735 (1999).

[23]T. Vernay, Ph.D. thesis, École Polytechnique Fédérale de Lausanne, Switzerland (2009).

[24]T. Vernay, Ph.D. thesis, École Polytechnique Fédérale de Lausanne, Switzerland (2012).

[25]M. N. Rosenbluth and F. L. Hinton, Phys. Rev. Lett. **80**, 724 (1998).

47

[26] X. Lapillonne, Ph.D. thesis, Ecole Polytechnique Fédérale de Lausanne, Switzerland (2010).

[27] A. Burckel, O. Sauter, C. Angioni, J. Candy, E. Fable, and X. Lapillonne, Journal of Physics: Conference Series **260**, 012006 (2010).

[28] A. J. Brizard, Communications in Nonlinear Science and Numerical Simulation **13**, 24 (2008), ISSN 1007-5704, vlasovia 2006: The Second International Workshop on the Theory and Applications of the Vlasov Equation.

[29] A. J. Brizard, Journal of Physics: Conference Series **169**, 012003 (2009).

[30] L. Villard, B. F. McMillan, O. Sauter, F. Hariri, J. Dominski, G. Merlo, S. Brunner, and T. M. Tran, Journal of Physics: Conference Series **561**, 012022 (2014).

[31] T. S. Hahm, Physics of Plasmas **1**, 2940 (1994).

[32] L. Villard, A. Bottino, O. Sauter, and J. Vaclavik, Physics of Plasmas **9**, 2684 (2002).

[33] M. Fivaz, Ph.D. thesis, École Polytechnique Fédérale de Lausanne, Switzerland (1997), thesis number 1692.

[34] J. Dominski, S. Brunner, S. K. Aghdam., T. Görler, F. Jenko, and D. Told, J.Phys:Conf.Ser. **401**, 012006 (2012).

Appendix A: Matrix assembly in discrete Fourier representation

In ORB5, the field is represented with BSplines[6,9]

$$\delta\phi(s,\theta^\star,\varphi) = \sum_{i=1}^{n_s+d}\sum_{j=1}^{n_\theta}\sum_{l=1}^{n_\varphi}\sum_{m=1}^{n_\theta}\sum_{n=1}^{n_\varphi}\delta\hat{\hat{\phi}}_{(i,m,n)}e^{\imath(m\theta^\star_j+n\varphi_l)}$$

$$\times \Lambda_i(s)\Lambda_j(\theta^\star)\Lambda_l(\varphi), \quad \text{(A1)}$$

and the QNE (11) is transformed into a system of toroidally decoupled equations[6,9]

$$\sum_n\sum_{i',m'}L_{(i,m,n)(i',m',n)}\delta\hat{\hat{\phi}}_{(i',m',n)} = \hat{S}_{(i,m,n)}, \quad \text{(A2)}$$

where $\delta\hat{\hat{\phi}}_{(i',m',n)}$ (resp. $\hat{S}_{(i,m,n)}$) is the poloidal and toroidal discrete Fourier transform (DFT) of its finite element coefficients $\delta\phi_{(i',j',l')}$ (resp. $S_{(i,j,l)}$), with $\theta^\star_j = 2\pi j/n_\theta$ and $\varphi_l = 2\pi l/n_\varphi$. The system of equations (A2) is toroidally decoupled ($n = n'$) because the integrands of the integral equations (15), (16), (17), and (19) are composed of equilibrium quantities

independent of φ. The general form of the DFT of these toroidal integrals is

$$\hat{A}_{nn'} = n_\varphi^{-1} \sum_{l,l'} e^{-\imath n\varphi_l} \oint d\varphi \Lambda_l(\varphi)\Lambda_{l'}(\varphi + \Delta\varphi)e^{\imath n'\varphi_{l'}}$$

$$= \delta_{nn'}C^{(n)}(\Delta\varphi), \tag{A3}$$

where $C^{(n)} = \int_0^{2\pi/n_\varphi} d\varphi \hat{\Lambda}_n(\varphi)\hat{\Lambda}_n^*(\varphi + \Delta\phi)$ is such that one has the relation $C^{(n)}(\Delta\varphi = 0) = M^{(n)}$ with $M^{(n)} = \int_0^{2\pi/n_\varphi} d\varphi \hat{\Lambda}_n(\varphi)\hat{\Lambda}_n^*(\varphi)$ the toroidal mass matrix[6], and $\hat{\Lambda}_n(\varphi + \varphi_L) = \sum_l \exp(-\imath n\varphi_l)\Lambda_l(\varphi + \varphi_L) = \exp(-\imath n\varphi_L)\hat{\Lambda}_n(\varphi)$. The fact that the toroidal matrices are decoupled ($n = n'$) is proven by the presence of the Kronecker symbol, $\delta_{nn'}$, in Eq. (A3). The main rationale for using a DFT representation in the poloidal direction is to assemble these matrices by keeping only a subset of field-aligned poloidal modes[10], thus reducing the size of the matrices. For example, for a given toroidal mode number n, the turbulent field can be accurately represented by a sub set of "field-aligned" poloidal mode numbers $m \in [nq(s) - \Delta m, nq(s) + \Delta m]$ where $\Delta m \gtrsim 5$ typically and $q(s)$ is the safety factor.

The adiabatic response matrix, Eq. (15), is decomposed in two sub matrices, such that $L_{kk'}^{\text{ad}} = L_{kk'}^{\text{noFS}} + L_{kk'}^{\text{FS}}$ where $k = (i, m, n)$ is the triplet index. The matrices are

$$L_{kk'}^{\text{noFS}} = M^{(n)} \sum_{\sigma\in\{\text{ad}\}} q_\sigma^2 \sum_{I=1}^{n_s} \sum_Q w_Q \Lambda_i(s_I + s_Q)\Lambda_{i'}(s_I + s_Q)$$

$$\times \sum_q w_q \hat{\Lambda}_m(\theta_q^\star)\hat{\Lambda}_{m'}^*(\theta_q^\star)\hat{C}_{\sigma,m-m'}(s_I + s_Q, \theta_q^\star), \tag{A4}$$

and

$$L_{kk'}^{\text{FS}} = -M^{(n)} \sum_{\sigma\in\{\text{ad}\}} q_\sigma^2 \sum_{I=1}^{n_s} \sum_Q w_Q \frac{\Lambda_i(s_I + s_Q)\Lambda_{i'}(s_I + s_Q)}{2\pi\langle\mathcal{J}\rangle_{\theta^\star}(s_I + s_Q)}$$

$$\times \sum_q w_q \hat{\Lambda}_m(\theta_q^\star)\hat{C}_{\sigma,m}(s_I + s_Q, \theta_q^\star)$$

$$\times \sum_{q'} w_{q'} \hat{\Lambda}_{m'}^*(\theta_q^\star)\hat{\mathcal{J}}_{m'}^*(s_I + s_Q, \theta_{q'}^\star), \tag{A5}$$

where $\theta_J^\star = 2\pi J/n_\theta$, $\theta_q^\star = 2\pi q/(n_\theta n_q)$, I indexes the grid intervals associated to the regular knot sequence $s_I = (I - 1)/n_s$, s_Q are quadrature points over the interval $[0, 1/n_s]$, w_Q the associated quadrature weights, $\hat{C}_{\sigma,m}(s, \theta^\star) = \sum_{J=1}^{n_\theta} C_\sigma(s, \theta^\star + \theta_J^\star)\exp(-\imath m\theta_J^\star)$ with $C_\sigma(s, \theta^\star) = \mathcal{J}(s, \theta^\star)N_{\sigma0}(s, \theta^\star)/T_{\sigma0}(s, \theta^\star)$, $\hat{\mathcal{J}}_m(s, \theta^\star) = \sum_{J=1}^{n_\theta} \mathcal{J}(s, \theta^\star + \theta_J^\star)\exp(-\imath m\theta_J^\star)$, and $2\pi\langle\mathcal{J}\rangle_{\theta^\star}(s) = 2\pi \oint d\theta^\star \mathcal{J}(s, \theta^\star)$. For this matrix $\Delta\varphi = 0$ so that $C^{(n)}(\Delta\varphi = 0) = M^{(n)}$ without approximation.

The long-wavelength polarization matrix, Eq. (17), as well as the Padé correction matrix, Eq. (19), are assembled with

$$
\begin{aligned}
L_{kk'} = M^{(n)} \sum_{\sigma \in \{\text{kin}\}} \sum_{\{\alpha\beta\}} \sum_{I=1}^{n_s} \sum_{Q,q} & w_Q w_q \\
\times\, & \partial_\alpha [\Lambda_i(s_I + s_Q)\hat{\Lambda}_m(\theta_q^\star)] \\
\times\, & \partial_\beta [\Lambda_{i'}(s_I + s_Q)\hat{\Lambda}_{m'}^*(\theta_q^\star)]\, \hat{G}_{\sigma,m-m'}^{\alpha\beta}(s_I + s_Q, \theta_q^\star),
\end{aligned}
\tag{A6}
$$

where $\hat{G}_{\sigma,m}^{\alpha\beta}(s,\theta^\star) = \sum_{J=1}^{n_\theta} G_\sigma^{\alpha\beta}(s,\theta_J^\star + \theta^\star)e^{-\imath m \theta_J^\star}$ with $G_\sigma^{\alpha\beta} = m_\sigma g^{\alpha\beta}\mathcal{J}N_{\sigma 0}/B_0^2$ for the long-wavelength polarization matrix and $G_\sigma^{\alpha\beta} = (m_\sigma/q_\sigma^2)g^{\alpha\beta}\mathcal{J}T_{\sigma 0}/B_0^2$ for the Padé correction matrix. In Eq. (A6), one used the approximation $\nabla_\perp \simeq \nabla_{\text{pol}} = \nabla s \partial_s + \nabla\theta^\star \partial_{\theta^\star}$, the sum over $\{\alpha\beta\}$ is done for $\alpha\beta \in \{ss, s\theta, \theta s, \theta\theta\}$ with $g^{\alpha\beta} = \nabla\alpha \cdot \nabla\beta$. The approximation $\Delta\varphi \simeq 0$ and $C^{(n)} \simeq M^{(n)}$ are made.

The arbitrary-wavelength polarization drift matrix, Eq. (16), is assembled by assuming a local Maxwellian for the background distribution function

$$
f_{\sigma 0}(\mathbf{x}) = \frac{N_{\sigma,\text{eq}}(\mathbf{x})}{[2\pi T_{\sigma 0}(\mathbf{x})/m_\sigma]^{3/2}} \exp\left[-\frac{m_\sigma v_\parallel^2/2 + \mu B_0(\mathbf{x})}{T_{\sigma 0}(\mathbf{x})} \right].
\tag{A7}
$$

The polarization-drift matrix then reads

$$
\begin{aligned}
\hat{L}_{kk'}^{\text{pol}} = \sum_{\sigma \in \text{kin}} q_\sigma^2 \sum_{I,Q,J,q} & w_Q w_q \mathcal{J}(s_I + s_Q, \theta_J^\star + \theta_q^\star)\frac{N_{\sigma,\text{eq}}(s_I + s_Q, \theta_J^\star + \theta_q^\star)}{T_{\sigma 0}(s_I + s_Q, \theta_J^\star + \theta_q^\star)} \\
\times\, & \sum_{w=0}^{n_w-1} \Delta\tilde{v}_\perp\, \tilde{v}_{\perp,w} \exp\left(-\tilde{v}_{\perp,w}^2/2\right) \\
\times\, & \Bigg[\frac{1}{n_a} \sum_{a=1}^{n_a} M^{(n)} \Lambda_i(s_a)\hat{\Lambda}_m(\theta_a^\star)\Lambda_{i'}(s_a)\hat{\Lambda}_{m'}^*(\theta_a^\star) \\
- & \frac{1}{n_a^2} \sum_{a=1}^{n_a} \Lambda_i(s_a)\hat{\Lambda}_m^*(\theta_a^\star) \sum_{a'=1}^{n_a} C^{(n)}(\varphi_a - \varphi_{a'})\Lambda_{i'}(s_{a'})\hat{\Lambda}_{m'}^*(\theta_{a'}^\star) \Bigg],
\end{aligned}
\tag{A8}
$$

with a and a' the gyroaveraging quadrature points, n_a the number of these quadrature points which varies proportionally to $\tilde{v}_{\perp,w}$, $\tilde{v}_{\perp,w} = w\Delta\tilde{v}_\perp$, $n_w = \tilde{v}_{\perp,\text{max}}/\Delta\tilde{v}_\perp$ an input parameter of the simulation, and $\tilde{v}_\perp = v_\perp/v_{\text{th}}(s_I + s_Q, \theta_J^\star + \theta_q^\star)$. The quadrature over the perpendicular velocity is thus carried-out over a velocity grid which is systematically adapted to the local thermal velocity. To lighten the notation, the gyropoints coordinates have been noted $(s_a, \theta_a^\star, \varphi_a)$ when in fact they are function of other guiding-centre coordinates: $s_a = s(s_I + s_Q, \theta_J^\star + \theta_q^\star, \tilde{v}_{\perp,w}, \alpha_a)$, $\theta_a^\star = \theta^\star(s_I + s_Q, \theta_J^\star + \theta_q^\star, \tilde{v}_{\perp,w}, \alpha_a)$, and in case of the toroidal

angle only the difference $\varphi_a - \varphi_{a'} = \Delta\varphi(s_I + s_Q, \theta_J^\star + \theta_q^\star, \tilde{v}_{\perp,w}, \alpha_a, \alpha_{a'})$ is necessary for computing the integral. This difference is actually zero in our case, because we assemble the matrix in the approximation $\boldsymbol{\rho} \cdot \nabla\varphi = 0$. The term $C^{(n)}(\varphi_a - \varphi_{a'})$ is thus approximated by $C^{(n)}(\varphi_a - \varphi_{a'}) \simeq C^{(n)}(0) = M^{(n)}$. Finally, the computation of the gyropoints coordinates, in this approximation $\boldsymbol{\rho} \cdot \nabla\varphi = 0$, is described in Eq. (22).